CHAPTER

6

Nonpolar Cubic III-nitrides: From the Basics of Growth to Device Applications

Donat J. As and Klaus Lischka
University of Paderborn, Paderborn, Germany

6.1 INTRODUCTION

Commercially available group III-nitride-based optoelectronic devices are grown along the polar c direction, which suffer from the existence of strong "built-in" piezoelectric and spontaneous polarization. This inherent polarization limits the performance of optoelectronic devices containing quantum well or quantum dot (QD) active regions. To eliminate this problem, much attention has been focused upon the growth of non- or semipolar (Al, Ga, In) N. However, a direct way to eliminate polarization effects is the growth of cubic (100) oriented III-nitride layers. With cubic epilayers, a direct transfer of the existing GaAs technology to cubic III-nitrides will be possible and the fabrication of diverse optoelectronic devices will be facilitated. However, since cubic GaN is metastable and no cubic GaN bulk material exists in nature, heteroepitaxy, with all its drawbacks due to lattice mismatch, is necessary to grow this material. Due to the low lattice mismatch to cubic GaN, the substrate of choice for the growth of cubic III-nitrides is 3C-SiC (001).

In this paper, the latest achievements in the molecular beam epitaxy (MBE) of phase-pure cubic GaN, AlN, and their alloys grown on 3C-SiC (001) substrates are reviewed. A reflection high-energy electron beam (RHEED) control technique is presented to carefully adjust stoichiometry and to severely reduce the surface roughness and hexagonal inclusions. The absence of polarization fields in cubic nitrides is demonstrated and 1.55-μm intersubband absorption in cubic AlN/GaN superlattices is reported. The progress towards the fabrication of cubic GaN/AlGaN superlattices for terahertz applications is discussed and recent demonstrations of cubic III-nitride-based heterojunction field-effect transistors (HFET) with both normally off and normally on characteristics are summarized.

6.2 MOLECULAR BEAM EPITAXY OF CUBIC III-NITRIDES

Cubic group III-nitride samples were grown on 200-μm-thick, free-standing 3C-SiC (001) substrates by MBE (As, 2003; As et al., 2006). An Oxford Applied Research HD25 radio frequency plasma source was used to provide activated nitrogen atoms. Aluminium and gallium were evaporated from Knudsen cells. Prior to growth, the 3C-SiC (001) substrates were chemically etched by organic solvents and a buffered oxide etch and annealed for 10 hours at 500°C. Cubic GaN layers were deposited at 720°C directly on 3C-SiC substrates. The adsorption and desorption of metal (Ga and Al) layers on the c-GaN surface were investigated using the intensity of a RHEED as a probe. The structural and morphological properties of 3C-SiC substrates and group III-nitride epilayers were measured by high-resolution X-ray diffraction (HRXRD) and atomic force microscopy (AFM). Reciprocal space mapping (RSM) was performed to determine the Al molar fraction and the strain in the epilayers.

6.2.1 RHEED Control

As an important step to improve the GaN surface morphology in a systematic way, it is essential to

Molecular Beam Epitaxy.
DOI: https://doi.org/10.1016/B978-0-12-812136-8.00006-2

understand the surface structure and the underlying growth process on an atomic scale. In particular, the kinetic processes of adsorption and desorption on the surface are considered key parameters that govern the surface morphology, incorporation kinetics, and, consecutively, the overall material quality. In MBE of GaN, two-dimensional surfaces are commonly achieved under Ga-rich conditions, with theoretical (Northrup et al., 2000) and experimental (Koblmüller et al., 2005; Brandt et al., 2004) evidence suggesting that the growth front is stabilized by a metallic Ga adlayer. The optimum conditions for the epitaxial growth of c-GaN are mainly determined by two parameters, the surface stoichiometry and the substrate temperature (As, 2003, 2009). Both parameters are interrelated; therefore, an in-situ control of substrate temperature and surface stoichiometry is highly desirable. The study of the surface reconstruction by RHEED was one of the key issues in understanding the c-III-nitride growth (As, 2003; Schikora et al., 1996; Feuillet et al., 1997). First-principle calculations by Neugebauer et al. (1998) show that all energetically favoured surface modifications of the nonpolar (001) c-GaN surface are Ga-stabilized and therefore optimum growth conditions are expected under slightly Ga-rich conditions.

In Schörmann et al. (2007), in-situ RHEED was used to quantitatively determine the Ga coverage of the GaN surface during growth. Fig. 6.1 shows the RHEED intensity transient of the (0,0) reflection of the (2×2) reconstruction. After opening the Ga shutter, we observe a steep linear decrease of the RHEED intensity between I_o and the kink position (I_k). The gradient of the intensity drop is related to the impinging Ga flux. Using the known value of the Ga flux and the time Δt_k takes for the RHEED intensity to drop to I_k, we are able to calculate the amount of adsorbed gallium. Neglecting reevaporation of Ga we get a total number of adsorbed Ga atoms from the flux time $\Delta t_k \times (I_o - I_k)$ product. In all cases, this product is about $9.8\times10^{14}\,\mathrm{cm}^{-2}$, which is equal to the number of atoms of exactly one monolayer of Ga on the GaN surface (lattice constant of 4.52 Å). Since I_o is the reflectivity of the GaN surface and I_k is the reflectivity of GaN covered by one Ga monolayer, and the drop of the RHEED intensity in the time interval Δt_k is linear, the Ga coverage between 0 and 1 monolayer can be inferred from the measured intensity drop by linear interpolation. The decrease of the RHEED intensity below I_k is most likely due to further accumulation of Ga and thereby a modification of the Ga adlayer surface; however, it is not proportional to the amount of adsorbed Ga. For this reason, this method can only be used to measure the Ga coverage between zero and one monolayer, respectively. For Ga fluxes less than

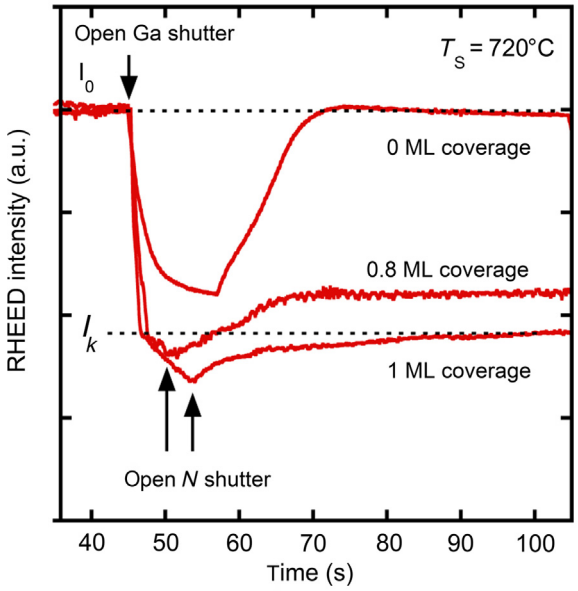

FIGURE 6.1 RHEED intensity transient measured during the growth of c-GaN, which started after opening the *N* source. The RHEED intensity measured during growth yields the amount of excess Ga (indicated in the figure) on the c-GaN surface. The Ga fluxes are 4.4×10^{14}, 3.2×10^{14} and $1.2\times10^{14}\,\mathrm{cm}^{-2}$ for the coverages of 1, 0.8 and 0 ML, respectively.

$3\times10^{14}\,\mathrm{cm}^{-2}\,\mathrm{s}^{-1}$, the situation is different. For these fluxes, it is not possible to define a kink position. The RHEED intensity drops to a certain value and saturates. Then desorption of Ga cannot be further neglected. After opening the N shutter, an increase of the RHEED intensity was observed, which is due to the formation of c-GaN. During further growth, the RHEED intensity saturates. From the saturation value, the Ga coverage can be calculated using I_k as a reference. This procedure allows measuring the Ga coverage in the range between 0 and 1 monolayer with an accuracy of 0.1 monolayer.

Fig. 11.2 shows the root-mean-square (RMS) roughness measured by a $5\times5\,\mu\mathrm{m}^2$ AFM scan of several c-GaN layers versus the Ga flux used during MBE. The nitrogen flux was kept constant for all samples. The corresponding values of the Ga coverage during growth, as measured by the procedure described above, are included in Fig. 6.2. Only values below one monolayer can be measured. Minimum roughness is obtained with one monolayer Ga coverage during growth.

It has variously been suggested that excess Ga acts as surfactant during the epitaxy of hexagonal GaN (Mula et al., 2001; Adelmann et al., 2002; Gogneau et al., 2004; Neugebauer et al., 2003). The data shown in Fig. 6.2 clearly demonstrate that this effect exists also on the (001) surface of c-GaN. The width of the

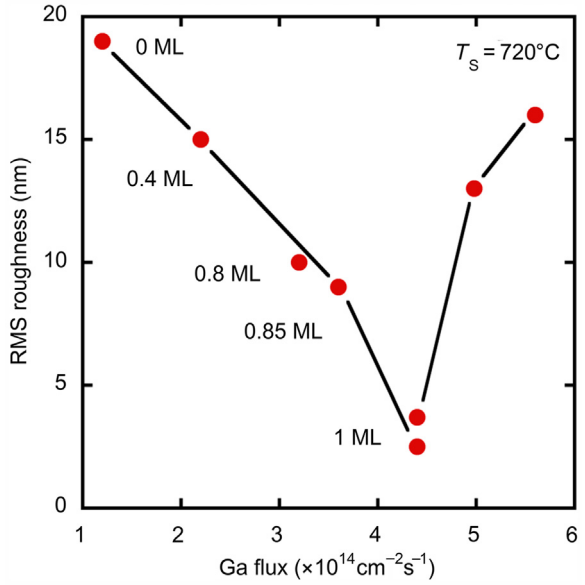

FIGURE 6.2 RMS roughness of c-GaN layers measured by $5 \times 5\,\mu m^2$ AFM scans vs Ga flux during growth. The corresponding values of the Ga coverage during growth are also included. Minimum roughness is obtained with an excess coverage of 1 ML. The line is a guide for the eyes.

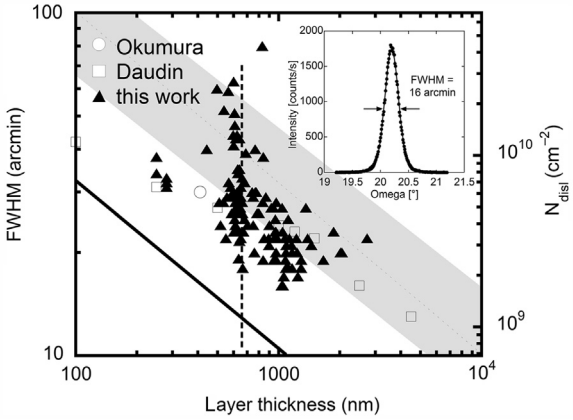

FIGURE 6.3 Rocking curve linewidth of cubic GaN epilayers grown on 3C-SiC substrates versus thickness of the cubic epilayers, respective data from c-GaN on GaAs are found in the shaded regime.

(002) X-ray rocking curve measured in double-axis configuration of 1-μm-thick c-GaN layers grown with one monolayer coverage is about 16 arcmin. Among c-GaN layers with equal thickness, 16 arcmin is a minimum value. Gallium fluxes, which are equivalent to a Ga coverage exceeding one monolayer, lead to a pronounced increase of the roughness and the full width at half maximum (FWHM) of the X-ray rocking curve.

6.2.2 Cubic GaN

HRXRD enables to measure the density of extended defects in epitaxial layers. The FWHM of the Bragg reflex obtained in a direction perpendicular to the diffraction vector (ω-scan) is related to the intensity of extended defects in the layer. The ω-scan measures the intensity spread for the coordinate $q_\perp$ in reciprocal space arising from both mosaicity and finite lateral domain size. Fig. 6.3 compiles HRXRD data from c-GaN layers with a varying thickness grown by MBE on GaAs (Lischka, 1997; Yang et al., 1996) and 3C-SiC (Okumura et al., 1997) substrates, respectively. A clear decrease of the FWHM with increasing layer thickness is seen and the values given in Yang et al. (1996) are quite comparable to our data. The linewidths measured for c-GaN grown on 3C-SiC substrates are approximately a factor of three narrower than those for layers grown on GaAs substrates. This may be expected due to the lower lattice mismatch of this system. The clear trend of decreasing FWHM with increasing layer thickness immediately implies that the number of extended defects is reduced in thicker epilayers.

In Fig. 6.3, the rocking curve line width (ω-scan) of all cubic GaN epilayers (full triangles) grown on 3C-SiC is plotted versus c-GaN layer thickness. Two effects can be clearly seen from this plot. First, a severe reduction of the FWHM with increasing epilayer thickness is observed. This linewidth dependence is consistent with the defect annihilation process observed in cubic GaN grown on GaAs (001) substrates (Yang et al., 1999). Since, in zinc-blende (ZB) structure, the stacking faults (SFs) lie on the (111) planes, an annihilation mechanism is possible when two SFs lying, e.g., on the (111) and on the (−1−11) planes, intersect and annihilate simultaneously with the creation of a sessile dislocation aligned along [110] directions. For the case of 3C-SiC, where the lattice mismatch is only −3.7% to cubic GaN, the full line shows the theoretical calculated FWHM as a function of layer thickness using the dislocation glide model by Ayers (1995). This model implies that the dislocation density N_{disl} is inversely proportional to the layer thickness d and that the FWHM is proportional to $d^{-1/2}$. In addition, with this model order-of-magnitude accuracy in quantitative predictions of the dislocation densities for a number of heteroepitaxial systems can be achieved. The full line through the 3C-SiC data shows this model calculation, which gives a relation between the dislocation density N_{disl}, the lattice misfit between substrate and epitaxial layer and the thickness of the epilayer. In the calculation, it was assumed that 60 degrees dislocations with a Burgers vector of 0.32 nm are the predominant defects in the layers. The trend of the calculated curve is in excellent agreement with the experimental data.

The estimated dislocation density N_{disl} is shown on the right-hand scale of the diagram. Comparing the full curve with the experimental data (full triangles), a reduction of the FWHM by a factor of 1.5 is still possible. By comparing these data with those cited in literature, the dependence of the FWHM on film thickness has to be taken into account. Up to now, only two other groups reported data on GaN on 3–5-μm-thick 3C-SiC/Si (001) pseudo-substrates grown by chemical vapour deposition (open circle Okumura et al. (1997) and open squares Daudin et al. (1998)). As can be seen in Fig. 6.3, we are clearly able to remain under the best-cited values, indicating the improved structural quality of our c-GaN epilayers due to the availability of free-standing bulk-like 3C-SiC (001) substrates. The HRXRD data are in good agreement with TEM investigations (Yang et al., 1996), which yield a defect density in the order of 10^9–10^{11} cm^{-2}. In addition, TEM measurements further showed that the density of stacking faults is drastically decreasing with increasing layer thickness. As mentioned above, the second parameter that strongly influences the quality of the cubic epilayers is the roughness of the 3C-SiC substrate. In Fig. 6.3, the linewidth of the rocking curve of 600-nm-thick cubic GaN epilayers on 3C-SiC substrates varies from 60 arcmin to 20 arcmin for substrates with different surface roughness (indicated by the vertical dashed line). The RMS roughness of the corresponding 3C-SiC substrates as measured by AFM on $5 \times 5\,\mu m^2$ large areas varied between 11 and 0.7 nm, respectively. The smoother the surface of the substrates are, the narrower the FWHM, and the higher the structural quality of the cubic epilayer. This observation is in agreement with measurements of Daudin et al. (1998) and indicates that further improvement of the surface preparation (atomic flat surfaces) may allow the achievement of the theoretical limit indicated by the full line. Up to now, the minimum X-ray rocking curve width of a 1-μm-thick c-GaN layer grown with 1 monolayer coverage was about 16 arcmin (see inset of Fig. 6.3), which is one of the best values reported so far.

For the sake of completeness, the shaded area in Fig. 6.3 depicts the range of FWHM values as measured for cubic GaN grown on GaAs substrates. However, the model of Ayers cannot be applied to heteroepitaxial systems with mismatch greater than about 10%, since in such systems the misfit dislocations are so closely spaced that the continuum elasticity theory cannot predict their line tension with acceptable accuracy. However, if we shift the calculated line upwards, one sees that, for the c-GaN/GaAs case, the same trend is observed (dashed line through shaded area). Therefore, the same defect annihilation process is also effective in the GaAs case. From the right-hand scale, we estimated a dislocation density of about 10^{10} cm^{-2} for a 1-μm-thick c-GaN epilayer on GaAs (001).

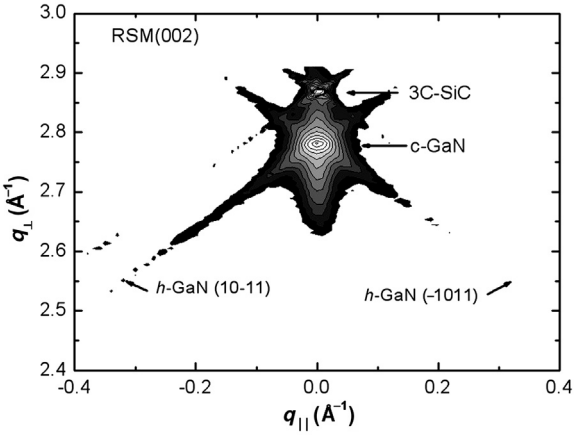

FIGURE 6.4 Reciprocal space map of a 600-nm-thick cubic GaN epilayer grown on 3C-SiC substrates. High-intensity (002) Bragg reflections of c-GaN and the 3C-SiC substrate are observed. Only a very weak (10–11) reflection from hexagonal GaN is measured yielding a content of hexagonal inclusions below 1%.

From experiments, it is well known that hexagonal inclusions mainly grow on (111) facets and cannot be detected by ω-2Θ scans. Therefore, RSM of the GaN (002) Bragg reflection were performed. The RSM of a 600-nm-thick cubic GaN epilayer on 3C-SiC substrate along the (−110) azimuth is shown in Fig. 6.4. Only a very weak intensity of the (10−11) and (−1011) reflections from hexagonal GaN (indicated in Fig. 6.4 by arrows) is measured, yielding a content of hexagonal inclusions below 1%.

6.2.3 Cubic AlN

AlN is a wide-band-gap semiconductor with a large thermal conductivity comparable to copper, a hardness close to sapphire, and a high chemical stability. Until recently, the metastable cubic phase of AlN had a considerable surface roughness, leading to short circuits and broadening of confined electronic states of low-dimensional structures (Daudin and Widmann, 1997; Lebedev et al., 2005). However, the PAMBE growth of atomically flat c-AlN layers on free-standing 3C-SiC substrate was reported recently (Schupp et al., 2010b). The growth procedure started with a deoxidation of the substrate. Surface oxides lead to blurred reflections of the cubic lattice; three-dimensional islands on the surface cause disc-shaped reflections due to an electron transmission component (Braun, 1999). After cleaning, the RHEED pattern of the 3C-SiC surface shows long thin streaks indicating a two-dimensional oxide-free surface with a (2×4) reconstruction and

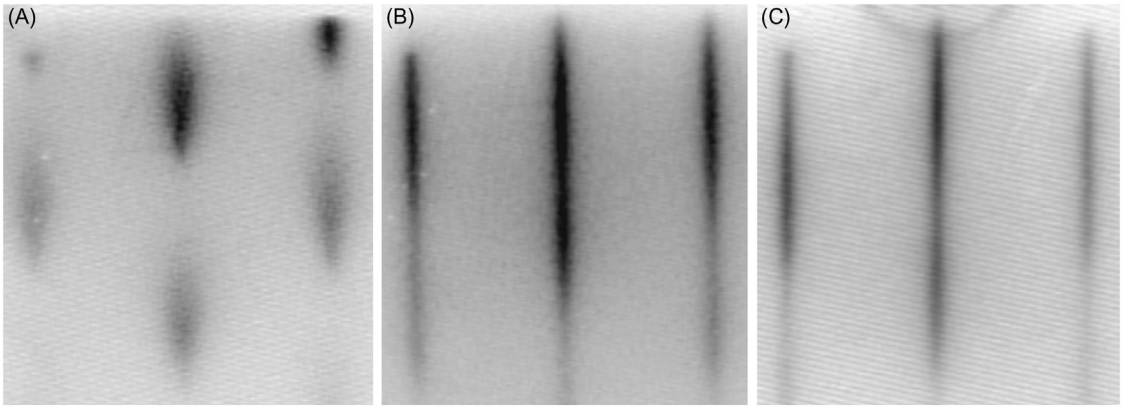

FIGURE 6.5 RHEED images of the c-AlN surface during the initial growth process: (A) after growth of 6 ML, (B) after growth of 30 ML and (C) after growth of 650 ML.

Kikutchi lines. More details on the cleaning process used can be found in Schupp et al. (2010b).

Exposing a c-AlN surface to nitrogen leads to the formation of hexagonal clusters. However, growing c-AlN with one monolayer Al surface coverage can prevent hexagonal condensation (Schupp et al., 2010b; Schörmann et al., 2006). Therefore, the c-AlN nucleation on the 3C-SiC substrate was done under one monolayer (ML) surface coverage of Al. The substrate temperature was 730°C and the Al beam flux was 2×10^{14} cm^{-2} s^{-1}, respectively. The growth was monitored in-situ by RHEED. At the initial growth process, a transition from 2D to a 3D surface was observed. This transition is clearly seen in Fig. 6.5 where the RHEED pattern after the deposition of 6 ML of c-AlN (Fig. 6.5A) is compared with that after deposition of 30 ML (Fig. 6.5B). The spotty reflections originating from an electron transmission component through islands on the surface are transformed into long streaks. After a smooth surface was established, growth interruptions of 30 seconds were applied every 20 atomic layers to avoid metal accumulation at the surface. RHEED intensity oscillations (not shown here) indicate a two-dimensional layer-by-layer growth and the growth rate was determined to be 0.2 ML/s. A smooth 2D surface is still seen after the growth of 142-nm (650 ML) c-AlN (see RHEED pattern in Fig. 6.5C).

The cubic structure of the AlN layer is clearly shown by HRXRD measurements. In Fig. 6.6, the HRXRD (113) reciprocal space map of a 300-nm c-AlN layer on 3C-SiC is shown. The peak of the arrow three indicates the position of the 3C-SiC Bragg reflection and the peak of arrow one indicates the position of the c-AlN reflection. The elliptic shape originates from a mosaic structure caused by strain relaxation (Holy, 1999). The main axis of the ellipse (white line in Fig. 6.6 labelled by 4) is perpendicular to the reciprocal lattice vector. A small shift of the c-AlN peak along the main axis can be interpreted as tilt of the c-AlN layer versus the substrate. Taking this tilt into account, the position of the c-AlN reflection is shifted to the peak position indicated by arrow two. The c-AlN lattice parameter in growth direction extracted from Fig. 6.6 is 4.373 ± 0.002 Å.

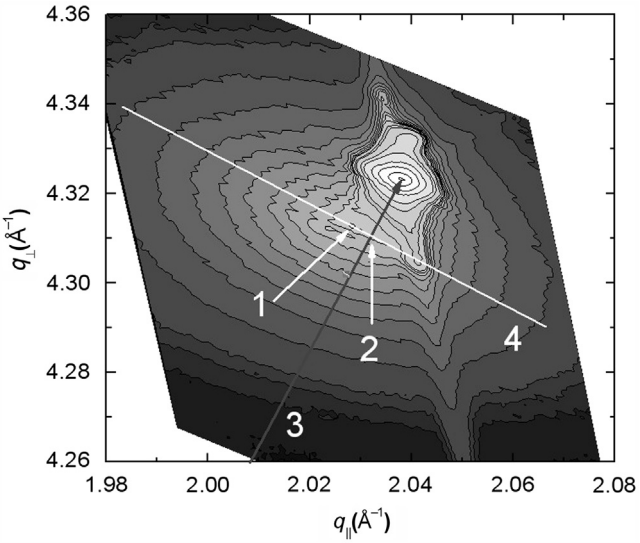

FIGURE 6.6 HRXRD reciprocal space map of the (113) reflections of c-AlN and 3C-SiC. (1) Position of the c-AlN peak, (2) position of c-AlN peak after tilt correction, (3) reciprocal lattice vector of 3C-SiC reflection, and (4) axis for tilt correction perpendicular to (3).

The high surface quality of the c-AlN layers is verified with AFM. The AFM image of the c-AlN layer shows an atomically smooth surface with a roughness of 0.2-nm RMS. The according line scan depicts a peak-to-valley height of only one lattice constant over a lateral extension of ~2000 lattice constants.

A commercial ellipsometer was employed for recording the ellipsometric parameters Ψ and Δ under different angles of incidence (Φ: 60, 67 and 74 degrees)

in the photon ($\hbar\omega$) energy range from 1 to 6.4 eV. A home-made construction attached to the Berlin Electron Storage Ring for Synchrotron Radiation (BESSY II) allowed measurements of Ψ and Δ under $\Phi = 67.5$ degrees from 5 to 10 eV with the set-up described in Cobet et al. (2009). The dielectric function (DF) was obtained by a multilayer fitting procedure similar to the approach presented in Goldhahn (2003). No assumption was made concerning the shape of the DF, i.e., the real (ε_1) and imaginary parts (ε_2) of the DF were separately fitted for all photon energies. Figs. 6.7A and B summarize the results of the fitting procedure for one of the cubic AlN films (layer thickness here was 100 nm). The spectral dependence shows similarities to the recently reported results for the hexagonal counterpart (Röppischer et al., 2009); however, the characteristic energies E_0, E_1 and E_2 differ appreciably.

The imaginary part of the DF exhibits a sharp onset at 5.88 eV, which defines the direct excitonic band gap. Adopting the exciton binding energy of 50 meV for the hexagonal AlN (Leute et al., 2009) the direct band gap (E_0) is determined at the Γ point of the Brillouin zone with 5.93 eV. This result is in excellent agreement with the calculated quasiparticle band gap of 5.86 eV if the lattice polarisability is taken into account (Leute et al., 2009). For comparison, previous studies of mixed-phase AlN yielded 5.74 eV for the ZB compound (Bechstedt et al., 2005). The pronounced absorption tail below 5.88 eV in Fig. 6.7B) is attributed to phonon-assisted indirect absorption. The imaginary part differs appreciably from zero only above 5.3 eV, i.e., this energy defines the upper limit of the indirect band gap. A slightly lower value might be possible as well, but ellipsometry is not sensitive enough in the case of low absorption. Finally, the E_1 and E_2 transition energies at room temperature amount to 7.20 and 7.95 eV, respectively.

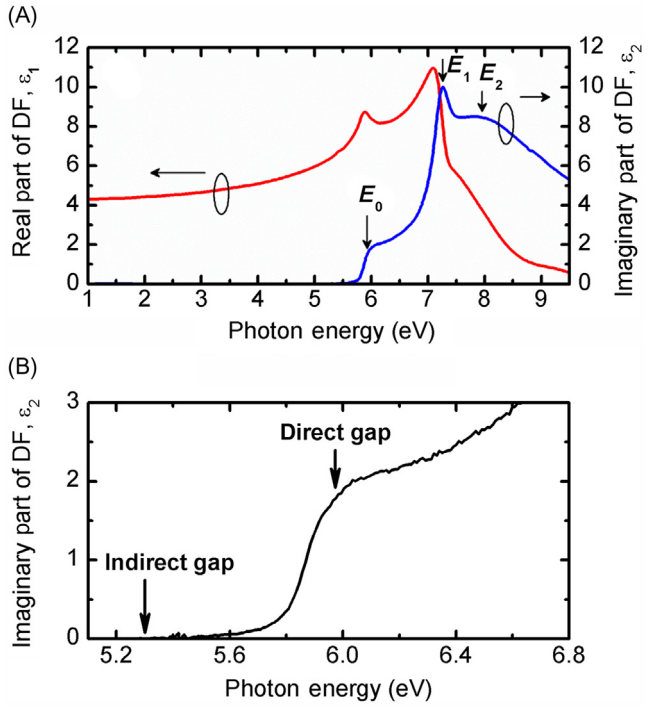

FIGURE 6.7 (A) Real and imaginary parts of the DF for c-AlN from 1 to 10 eV. (B) Magnification of the region close to the absorption edge.

6.2.4 Cubic AlGaN/GaN Quantum Wells

Cubic $Al_xGa_{1-x}N$ epilayers and cubic $Al_xGa_{1-x}N$/GaN MQW have been grown by MBE at 720°C. Such Al-containing epilayers are necessary for cladding layers in laser diodes or LEDs and are also used in resonant cavity LEDs for the realization of $Al_xGa_{1-x}N$/GaN distributed Bragg reflectors.

Fig. 6.8 shows the XRD ω-2Θ scan of the (002) Bragg reflection of a 15-period $Al_xGa_{1-x}N$/GaN MQW structure (upper curve). The reflections of the 3C-SiC substrate, of the c-GaN buffer as well as several superlattice peaks (SL − 5 to SL + 2) are clearly seen. This indicates a good $Al_xGa_{1-x}N$/GaN interface quality. The experimental data have been fitted using dynamic scattering theory (lower curve), yielding a well width of 10.2 nm, a barrier width of 10.8 nm and an Al mole fraction of $x = 0.3$. These values are in excellent agreement with data that were obtained from growth rate measurements using RHEED oscillation period. The appearance of RHEED oscillations after

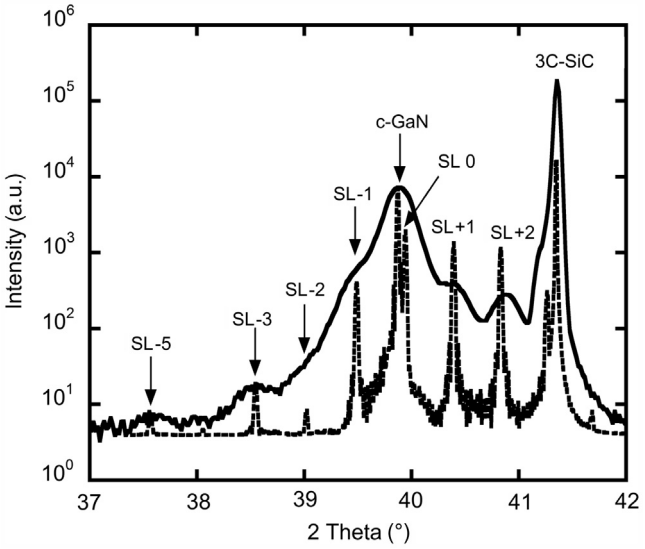

FIGURE 6.8 Measured ω-2Θ scan of $15 \times Al_{0.3}Ga_{0.7}N$/GaN MQW structure (solid line) and simulated data (dotted line). The well and the barrier width are 10.2 and 10.8 nm, respectively.

opening the Al shutter (Braun, 1999) emphasizes a two-dimensional $Al_xGa_{1-x}N$ growth mode at substrate temperatures of 720°C.

To demonstrate the absence of internal spontaneous polarization fields in cubic group III-nitrides, cubic single and multi- $Al_{0.15}Ga_{0.85}N$/GaN quantum wells were grown on 3C-SiC/GaN substrates (Schörmann et al., 2006). The quantum structures consist of 6-nm-thick $Al_{0.15}Ga_{0.85}N$ barriers and GaN wells with a width of 2.5–7.5 nm and were sandwiched between 50 nm AlGaN cladding layers. During growth of $Al_{0.15}Ga_{0.85}N$/GaN QWs, clear RHEED oscillations were observed allowing a stringent control of the growth rate and indicating two-dimensional growth of the respective layers. The room temperature photo luminescence spectra of a multiquantum well (MQW) structure excited with a HeCd-UV laser is shown in the inset of Fig. 6.9. The dimensions of the quantum structures are 3-nm-thick wells and 6-nm barriers. A strong emission is observed at 3.30 eV, which lies between the c-GaN emission at 3.2 eV and the emission of the $Al_{0.15}Ga_{0.85}N$ cladding layer at about 3.48 eV (As et al., 2003). The PL linewidth of the cubic QW luminescence is about 103 meV and is almost comparable to values reported for nonpolar hexagonal AlGaN/GaN quantum wells (Craven et al., 2004). The slightly broader linewidth in the cubic structures is attributed to the higher density of dislocations.

Fig. 6.9 depicts the dependency of the QW emission energy on the well width for both cubic (blue squares) and hexagonal QWs (red dots). Therein, the shift in transition energies compared to the band-gap energy is plotted versus well width. For our cubic $Al_{0.15}Ga_{0.85}N$/GaN QWs, the peak energy of the emission exactly follows the square-well Poisson–Schrödinger model and demonstrates the absence of polarization-induced electrical fields. For comparable hexagonal $Al_{0.17}Ga_{0.83}N$/GaN QWs on sapphire substrates, the experimental data can only be explained if an internal spontaneous electrical field of 750 kV cm^{-1} is taken into account (Grandjean et al., 1999). These results indicate that the well-known thermodynamic metastability of the cubic nitrides does not necessarily limit their application for polarization-free structures.

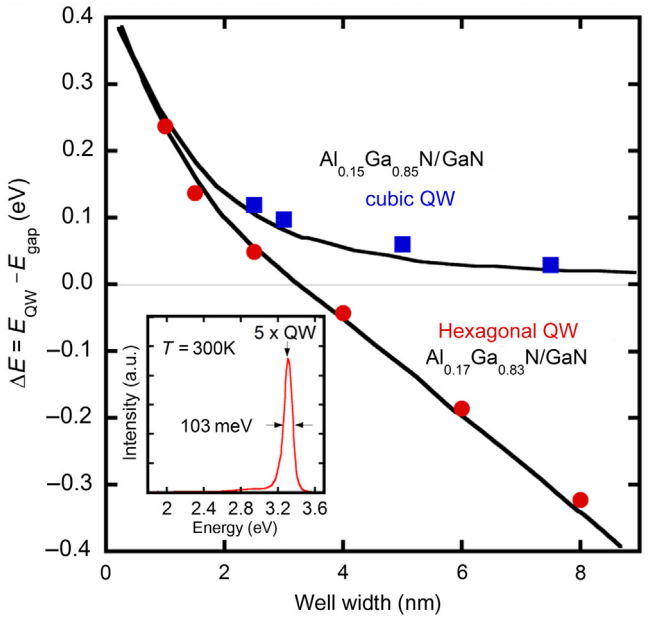

FIGURE 6.9 Transition energies of $Al_{0.15}Ga_{0.85}N$/GaN MQWs versus well width for cubic (blue squares) and hexagonal (red dots) MQWs. The squares and dots are experimental data; the curves are calculated using a self-consistent Poisson–Schrödinger model. For the hexagonal QWs, an internal field of 750 kV cm^{-1} is estimated. Inset: Room temperature photoluminescence spectrum of a cubic MQW.

6.2.5 Cubic GaN Quantum Dots

Due to a large exciton-binding energy and their large band offsets, GaN QDs are promising solid state emitters for devices operating at high temperature, such as nanolasers, single photon sources, and quantum information devices. Although less mature than their group-III ar- senide counterparts, a good understanding of self-assembled polar wurtzite-phase (WZ) GaN QDs has been reached with evidences of their exciton fine structure (Kindel et al., 2010), as well as thorough studies of their polarization properties (Bardoux et al., 2008), and their biexciton behavior (Kako et al., 2004; Simeonov et al., 2008; Kindel et al., 2009). Moreover, polar GaN QDs have already been proven to behave as single photon emitters up to 200K (Kako et al., 2006). However, the potential of such self-assembled polar QDs is hindered by the presence of a giant built-in electric field that extends their radiative lifetime (Kako et al., 2003; Bretagnon et al., 2006) and broadens their spectral linewidth via an enhanced spectral diffusion (Bardoux et al., 2006). Besides, the presence of an intense acoustic phonon sideband (Ostapenko et al., 2012) suggests that the destruction of phase coherence by phonon scattering would limit their use in quantum information applications. Because of the absence of spontaneous polarization in the ZB phase of group-III nitrides, ZB GaN QDs are a good alternative to their WZ counterpart and should exhibit reduced spectral diffusion and much shorter radiative lifetimes (Simon et al., 2003). The growth of ZB GaN QDs has been originally demonstrated by plasma-assisted MBE in the frame of the Stranski–Krastanov (SK) growth mode (Martinez-Guerrero et al., 2000). More recently, a droplet epitaxy

(DE) technique has also been developed which allows for greater control of the QD density (Schupp et al., 2010a,c).

Stranski–Krastanov growth was performed in a Riber 32 MBE system adapted with standard effusion cells for Ga and Al evaporation on 10 μm (001) 3C-SiC substrates on top of 500 μm Si (Bürger et al., 2015). Atomic nitrogen was provided by an Oxford plasma source and the growth process was in situ controlled by RHEED. Prior to the growth the substrate was cleaned by Al flashes at 910°C substrate temperature (Schupp et al., 2010d). After cooling down the substrate to a growth temperature of 760°C, the growth of a 30 nm c-AlN buffer layer was initiated. Since the c-AlN layer with a lattice constant of $a = 4.37$ Å (Schupp et al., 2010d) is pseudomorphically strained on 3C-SiC ($a = 4.36$ Å (Taylor and Jones, 1960)), a lattice mismatch of ~3.2% between c-GaN ($a = 4.50$ Å) (Strite et al., 1991) and the buffer layer enables the creation of self-assembled QDs by the strain-driven SK process. The three dimensional island formation is indicated by a transition from a streaky to a spotty RHEED pattern (Schupp et al., 2010a). Prior to the QD formation a two dimensional layer c-GaN is expected to be deposited in the Frank–Van der Merwe growth mode (Frank and Van der Merwe, 1949). To obtain data from the QDs by AFM measurements, the samples were immediately cooled down after the QD formation. For the optical characterization by PL measurements QDs are covered by a 30 nm c-AlN cap layer. Details of the c-AlN and c-GaN QD growth procedure with corresponding RHEED patterns are described in (As, 2009; Schupp et al., 2010d; Bürger et al., 2012).

The amount of deposited GaN varied from 2–4 monolayers (MLs). Taking into account delay times of the shutters and a deposition time of 0.2 ML/s, the accuracy of the deposited amount of GaN was estimated to ± 0.2 MLs. AFM scans were performed using a Nanosurf Mobile S system in contact mode on uncapped samples to obtain the surface morphology. The surface morphology of two uncapped samples with different amounts of deposited GaN is compared in Fig. 6.10. The $1 \times 1\ \mu m^2$ AFM scan in Fig. 6.10A reveals a high QD density of $1.2 \times 10^{11}\ cm^{-2}$, formed by 3 MLs GaN. The average width of the QDs is ~24 nm with a height of ~2.2 nm. Regarding Fig. 6.10B 2 MLs GaN were deposited resulting in a QD density of $1.5 \times 10^{10}\ cm^{-2}$. The average width and height of the QDs is ~11 nm and ~1.4 nm, respectively. Above 3 ML GaN deposition the coalescence of QDs appears hindering an accurate determination of the QD density and dimensions.

Regarding the PL experiments, the capped samples were excited by a frequency quadrupled Nd:YAG CW laser at 266 nm with an output power of 5 mW. Uncapped c-GaN QDs samples do not show luminescence. The laser spot is focused to ~200 μm diameter to collect ensemble luminescence data from the QDs. A photomultiplier mounted at a Spex 270 M monochromator was utilized for photon detection. Room temperature PL spectra of c-GaN QDs in the range of 3–4.65 eV are shown in Fig. 6.11. Due to the delta function, like density of states, the optical transitions of QDs are expected to be atom like. With respect to the large number of excited QDs, the observed PL spectra are formed by superimposed individual

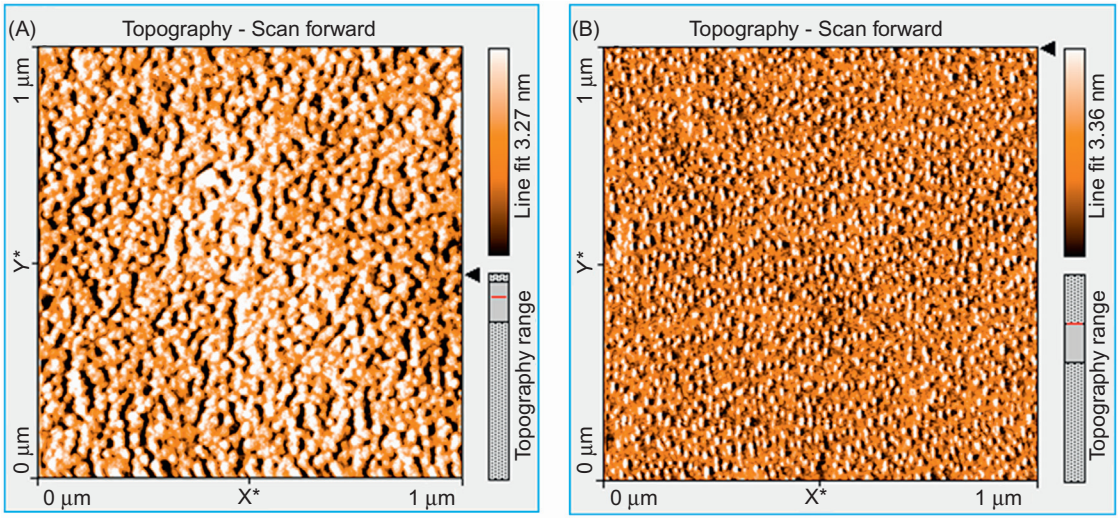

FIGURE 6.10 $1 \times 1\ \mu m^2$ AFM scans of (A) high density QDs ($1.2 \times 10^{11}\ cm^{-2}$) and (B) low density QDs ($1.5 \times 10^{10}\ cm^{-2}$) formed by 3 and 2 MLs GaN, respectively.

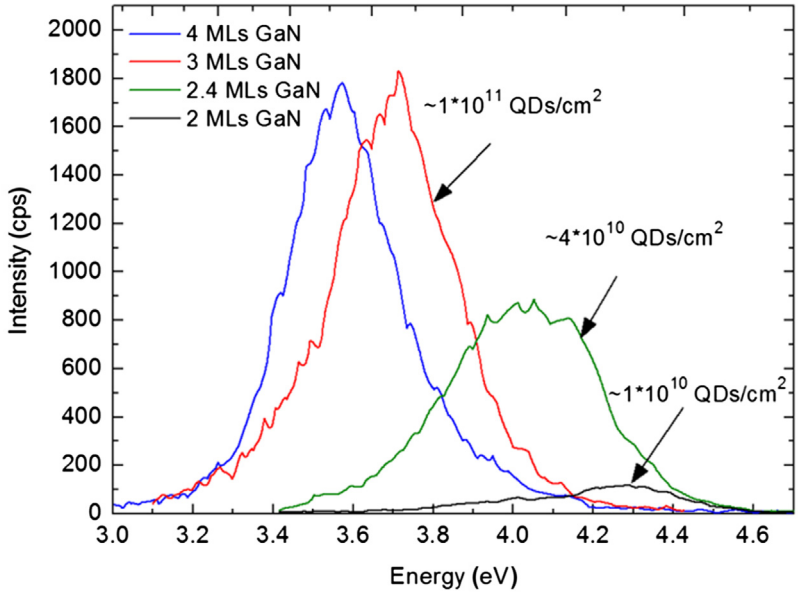

FIGURE 6.11 Room temperature PL spectra of c-GaN QDs ensembles in the range of 3–4.65 eV. The amount of nominally deposited GaN is varied from 2 to 4 MLs corresponding to QD densities from $\sim 1 \times 10^{10}$ to $\sim 1 \times 10^{11}$ cm^{-2}.

Gaussian shaped emission bands of many single QDs affected by an unintentional size distribution (Schmid, 2006). The confinement energy of c- GaN QDs in c-AlN leads to transition energies much larger than the band gap energy of bulk c-GaN (As et al., 1997). The increase of the peak intensity by one order of magnitude with increasing GaN deposition is attributed to an increase of the QD density within the same range (see Fig. 6.10). Between 3 and 4 MLs GaN deposition at almost constant peak intensity, reveals no significant change in the QD density, but an increase of the QD size (decreasing peak emission energy). By increasing the amount of deposited GaN, a redshift of the emission energy from 4.25 eV (2 MLs) to 3.56 eV (4 MLs) is observed. This decrease of the emission energy indicates again an increase of the QD size, as obtained by AFM of uncapped QDs (see Fig. 6.10). Calculations of the exciton transition energy in c-GaN QDs identified the QD height as the main confinement parameter (Fonoberov and Balandin, 2003).

The redshift of the emission energy agrees with these calculations of the emission energy as a function of the QD height. In the PL spectrum of the 2 MLs GaN sample (black curve), a low energy tail can be observed, which may be caused by a bimodal QD size distribution. The high emission energies around 4 eV in Fig. 6.11 are related to very small QDs, which are close to the resolution limit of AFM (cf. Fig. 6.10). The Gaussian shaped ensemble emission bands are a superposition of individual QD emission lines and its FWHM can be used to estimate the QD size distribution (Schmid, 2006). The FWHM decreases from 439 meV (2.4 MLs GaN) to 351 meV (3 MLs GaN) indicating changes in the QD size distribution.

The data obtained from AFM scans were correlated with the PL results. Fig. 6.12 illustrates the analysis of the QD density *pi* as a function of the GaN coverage Θ. The AFM data (black squares) and the integral PL intensities (red dots) are plotted versus the amount of deposited GaN in Fig. 6.12. Both diagrams show an abruptly increase above 2 MLs. To verify the QD formation mechanism, the experimental data are compared with an analytical model developed by Leonard et al., Leonard et al. (1994). This simple empirical model was originally developed for the analysis of self-assembled InAs QDs on GaAs and in the meantime applied to many other QD systems. It reveals the SK process as the main formation process and is also suitable to determine the critical layer thickness Θ*c*. The QD density *pi* is expressed as a function of the surface coverage Θ by

$$pi = p_0(\Theta - \Theta c)\alpha \tag{6.1}$$

Using $p_0 = 1 \times 10^{11}$ cm^{-2} and an exponent of $\alpha = 0.7$, the model matches reasonably well with the experimental data, as shown by the solid line in Fig. 11.12 and confirms thereby the formation of self-assembled QDs by the strain-driven SK mechanism. Furthermore, the critical layer thickness Θc can be determined to 1.95 MLs (see extrapolated dashed line in Fig. 6.12.). After reaching the critical layer thickness 3D islands are created to reduce strain and surface energy of the pseudomorphic grown GaN layer (Stranski and Krastanow, 1937). These results are in good agreement with similar results reported for other semiconductor systems and clearly evidence the formation of QDs by the SK process (Leonard et al., 1994; Schikora et al., 2000; Arakawa et al., 2003).

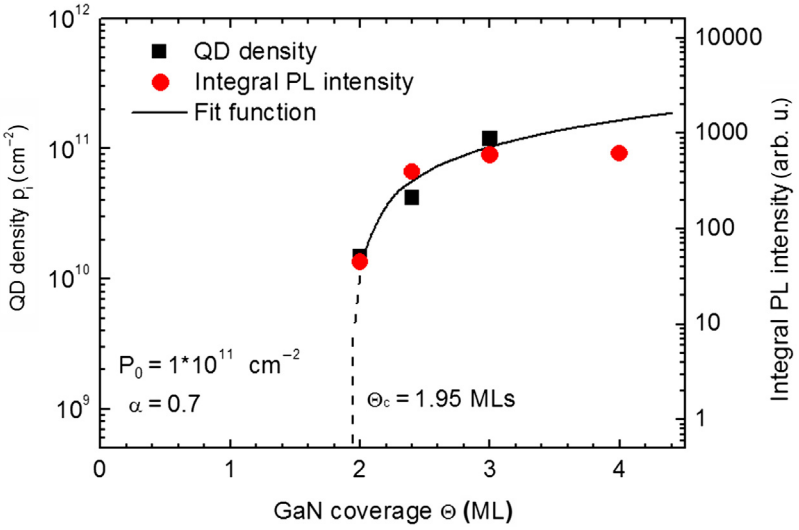

FIGURE 6.12 Room temperature PL QD density (black squares) as a function of GaN coverage correlated with the integral PL intensities (red dots) from Fig. 11.10. The QD densities are obtained by AFM scans. The solid line indicates a fit function according to Eq. (6.1).

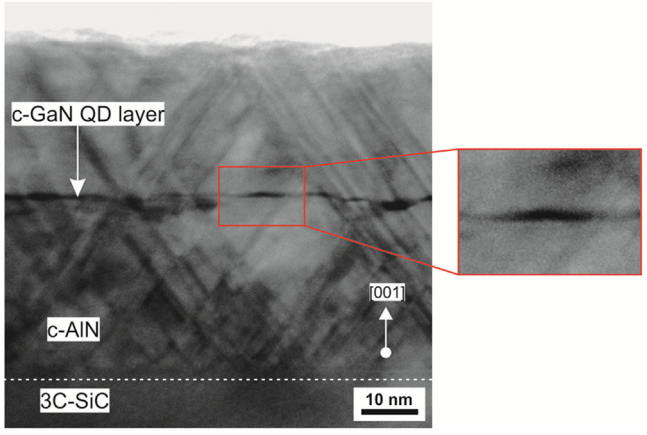

FIGURE 6.13 TEM image in cross-section geometry of the active c-AlN/c-GaN QD layer. The red rectangle shows a more detailed image of a single c-GaN QD. The white border lines of the magnified QD shows the assumed QD shape of Fonoberov and Balandin (2003) as a guide for the eyes.

To gain further insight in capped QDs, an additional sample with a single layer of SK QDs with the amount of 2.4 MLs GaN was grown for TEM imaging. For TEM studies at buried c-GaN QDs a JEOL

FX2000 microscope was used at 200 keV. In Fig. 6.13 a bright-field cross- sectional TEM image of the capped QD layer structure with high magnification is displayed. In the lower part, the interface between the 3C-SiC substrate and the c-AlN buffer layer is highlighted by a white dashed line. This interface has been previously analyzed by HRTEM and is atomically sharp (Kemper et al., 2014). Between the c-AlN buffer and cap layer (brighter areas) a thin single layer of c-GaN QDs (dark areas) is apparent. The red rectangle magnifies a single QD in a defect free environment. As a guide for the eyes, the white border lines indicate a truncated pyramid shape for the proposed c-GaN QD similar to the shape used for the calculations of the transition energies in Fonoberov and Balandin (2003). The dimensions of the QD can be roughly estimated to a diameter of 10–15 nm and to a height of ~1.5 nm. The thickness of the c-AlN layers are measured to ~32 nm.

An alternative method for the growth of c-GaN quantum is the DE, essentially a vapour–liquid–solid process. In DE, liquid Ga droplets are created and subsequently nitridated to form GaN QDs (Koguchi, 2007). DE has the advantage of size and density control of the QDs in a wide range from 5×10^8 to 5×10^{12} cm^{-2}. Especially the low density is of great importance for applications as single-photon emitters. Here the minimum spatial separation of the QDs has to be in the order of the emission wavelength.

The fabrication of the c-GaN DE QDs begins with the deposition of a defined amount of Ga, equivalent to 1–12 ML. The formation of Ga droplets is induced by the strong cohesion force between the Ga atoms. The distance between the Ga droplets is governed by two main factors, the amount of deposited Ga and by the surface diffusion length, the latter controlled by the substrate temperature (Sanorpim et al., 2007). For this sample series an AlN surface temperature of 350°C was used. In the next step, the Ga droplets are nitridated by exposure to the N plasma beam for 3–15 minutes while ramping up the substrate temperature from 350°C to 730°C. Fig. 6.14 shows the RHEED pattern of (A) reflections of the c-AlN layer, (B) reflections of c-GaN droplet QDs, the spotty reflections indicate 3D islands of cubic crystal structure, of (C) reflections of the c-AlN layer after 4 ML QD overgrowth, the smaller FWHM of the spotty reflections indicate partially strained GaN QDs and (D) reflections

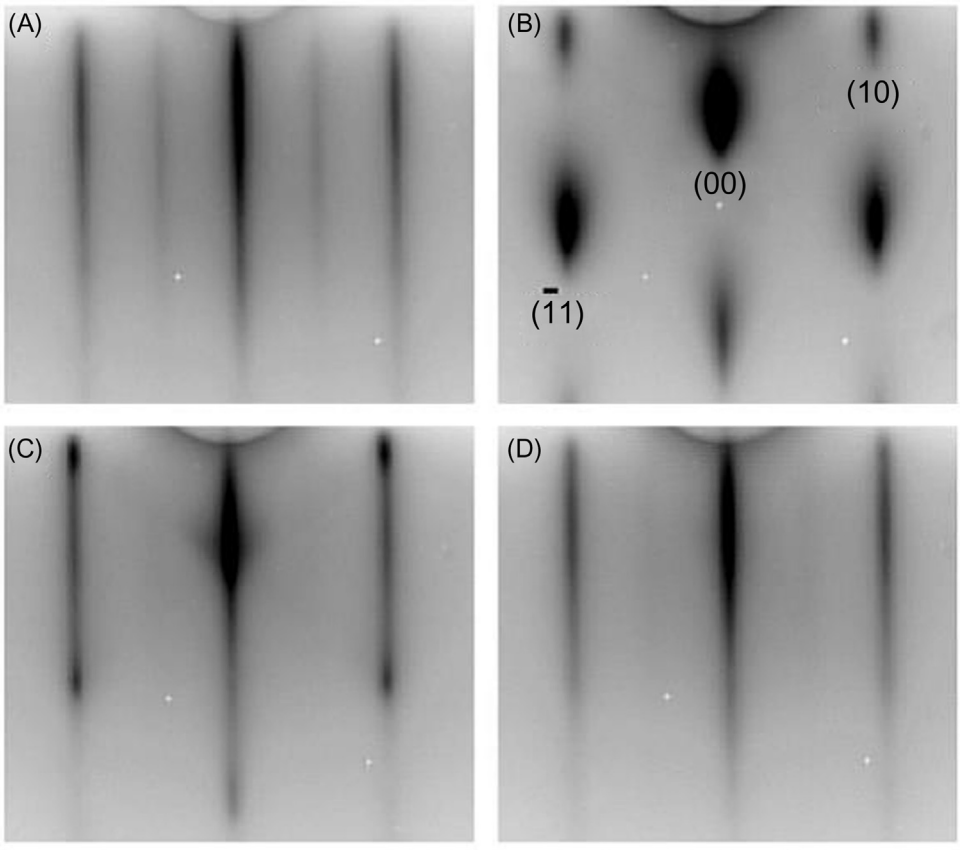

FIGURE 6.14 RHEED patterns: (A) reflections of the c-AlN layer, long thin streaks indicate a smooth 2D surface. (B) Reflections of c-GaN droplet QDs, the spotty reflections indicate 3D islands of cubic crystal structure. (C) Reflections of the c-AlN layer after 4 ML QD overgrowth, the smaller FWHM of the spotty reflections indicate partially strained GaN QDs. (D) Reflections of the c-AlN after 30 ML QD overgrowth, long thin streaks indicate a smooth 2D surface.

of the c-AlN after 30 ML QD overgrowth. Similar to the case of SK QDs spotty reflections indicate QDs on the surface. As all reflections in the RHEED pattern can be attributed to the ZB lattice structure, cubic phase purity can be concluded within detection limits (Sanorpim et al., 2007). In the final step, the c-GaN QDs are overgrown by a 30 nm c-AlN barrier layer at 730°C substrate temperature. Fig. 6.14D shows the RHEED pattern of the AlN surface after QD overgrowth with long thin streaks and the absence of spotty reflections. As a result, a smooth surface with full epitaxial overgrowth of the GaN QDs can be followed. AFM verifies the smooth AlN surface after GaN QD overgrowth.

6.3 DEVICE APPLICATIONS OF CUBIC III-NITRIDES

The group III-nitrides became the well-established material basis for a number of optoelectronic and electronic devices. The thermodynamically stable, hexagonal phase of these semiconductors is predominantly grown on the c-plane surface of sapphire or SiC, which, as a consequence of the crystal symmetry, leads to the inherent formation of spontaneous and piezoelectric polarization fields which can be detrimental for some device applications (e.g., MQWs for terahertz emitters). Therefore, the growth of so-called nonpolar and semipolar structures has attracted growing interest in the last years. This may be done by using *a*- or *m*-plane substrates for the preparation of hexagonal III-nitrides or to grow cubic-phase III-nitrides, which may be considered as the real nonpolar modification of this class of materials. In the following, recent activities are summarized to realize various device concepts, which take advantage of the absence of polarization fields.

6.3.1 Cubic AlN/GaN Quantum Wells for Intersubband Spectroscopy

Progress in hexagonal III-nitride epitaxial growth has extended the optoelectronic applications of this

material system from the ultraviolet region to the near-infrared spectral region (DeCuir et al., 2006; Hofstetter et al., 2006; Guillot et al., 2006; Baumann et al., 2005; Ridley et al., 2003; Suzuki et al., 2003; Vurgaftman et al., 2001). The ability to engineer quantum-well structures consisting of $Al_{1-x}Ga_xN$ and GaN over a wide spectral range was made possible by the considerable conduction band offset between the two binaries AlN and GaN (~1.8 eV) (Vurgaftman et al., 2001). It is the magnitude of this band offset that theoretically enables the tuning of intersubband (ISB) transition wavelengths towards the technologically important wavelengths such as 1.55 μm. Great strides in understanding the growth kinetics of hexagonal nitride materials has enabled steady progress in the growth and fabrication of detectors based on the intersubband transitions in GaN/AlN-based systems (Hofstetter et al., 2006; Guillot et al., 2006; Baumann et al., 2005; Morkoc, 1999; Andersson et al., 2007). However, the large built-in electrostatic fields in polar hexagonal heterostructures grown on c-plane (0001) sapphire strongly influence their optical and electrical properties (Ambacher et al., 1999; Park and Chuang, 2000). Efforts to circumvent these effects have been accomplished using R-plane $(10\bar{1}2)$ sapphire substrates, which result in nonpolar *a*-plane $(10\bar{1}2)$ hexagonal nitride material, thus effectively eliminating the contributions of these polarization fields (Gmachl and Ng, 2003; Kuokstis et al., 2005).

On the other hand, spontaneous polarization and piezoelectric fields do not exist in cubic GaN/AlN heterostructures and quantum wells. Thus, it was of interest to investigate the intersubband transitions in this particular cubic GaN/AlN quantum structure. The optical absorption due to the intersubband transition in nonpolar cubic GaN/AlN short-period superlattices grown by plasma-assisted MBE on 3C-SiC substrates has first been reported by E.A. DeCuir et al. DeCuir et al. (2008). All quantum structures were grown at 720°C on free-standing 3C-SiC (001) substrates by plasma-assisted MBE. A 100-nm-thick c-GaN buffer was deposited on a 3C-SiC substrate using the RHEED control of the growth process (Schörmann et al., 2007). Subsequently, a 20-period GaN/AlN superlattice (SL) was grown. The barrier thickness was fixed at 1.35 nm for all samples, while the well thickness was varied in the range between 1.6 and 2.1 nm. Finally, the quantum structures were capped with a 100-nm-thick c-GaN layer. To increase the optical absorption length, the samples were cut into waveguide geometry to allow for multiple passes. Inter-subband transitions were then observed in absorption spectra in the range of 1.5−2 μm. The experimental results are summarized in Table 6.1. They are found to be in good agreement with peak energies calculated as a function of the well width using a propagation matrix method. Good agreement was obtained between the calculated and measured values (DeCuir et al., 2008).

The intersubband absorption of cubic GaN/Al(Ga)N QW superlattices in a wider spectral range was reported by Machhadani et al. (2011). By varying the QW thickness and Al content, it was possible to tune the ISB absorption wavelength from 1.4 μm to even 63 μm (~4.8 THz). This corresponds to the shortest and the longest ISB wavelength ever achieved with this material system.

A typical transmission spectrum for TM-(*p*-) and TE-(*s*-) polarized light is shown in the inset of Fig. 6.15. The spectrum is normalized by the response of the optical system. The oscillations observed in the spectrum arise from the Fabry−Perot interferences in the 10-μm-thick SiC layer. The high-energy cut-off corresponds to the absorption of the Si substrate, whereas the low-energy transmission drop at 0.21 eV corresponds to the two-phonon absorption of the SiC template. An absorption peak at 0.46 eV is observed for TM-polarized light, which is a clear signature of an ISB resonance.

Fig. 6.15 displays the ISB absorption spectra of three different samples together with the corresponding Gaussian fits. The absorption peaks are at 1.4 μm (sample A), 2.7 μm (sample B) and 4.1 μm (sample C),

TABLE 6.1 Summary of the 20-period Cubic GaN/AlN Superlattice Samples Used in the Present Study. The period is obtained from the high-resolution X-ray diffraction, L_W (nm) is the well width, E_{peak} is the peak position energy obtained from the experimental measurements, FWHM is the full width at half maximum of the intersubband transition spectra, n_{2D} is the two-dimensional electron gas obtained by electrochemical capacitance measurements and E_F is the Fermi energy level

			E_{peak} (meV)				
Sample Number	**Superlattice Period (nm)**	**L_W (nm)**	**Measured**	**Calculated**	**FWHM (meV)**	**n_{2D} (10^{11} cm^{-2})**	**E_F (meV)**
A	3.45	2.1	620	630	182	2.79	3.52
B	3.1	1.75	696	734	211	2.33	2.94
C	2.95	1.6	751	781	219	2.13	2.68

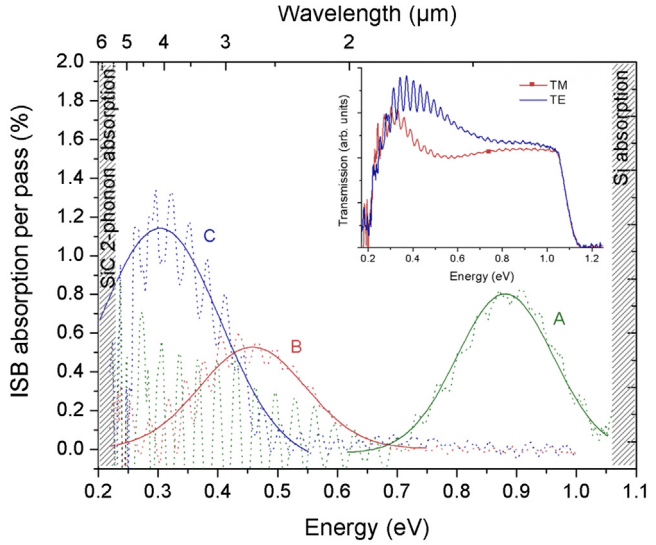

FIGURE 6.15 Room temperature TM absorption (characteristic of ISB transitions) per pass in the active region of three samples A, B and C (dotted curves) and corresponding Gaussian fits (full curves). Inset: Room temperature infrared transmission spectrum of sample B for TM- and TE-polarized light.

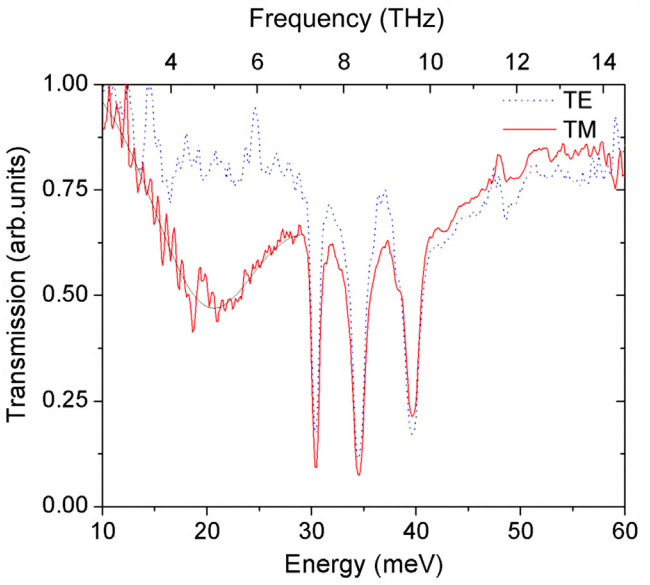

FIGURE 6.16 Low-temperature far-infrared transmission spectrum of an $Al_{0.05}Ga_{0.95}N/GaN$ MQW structure for TM-polarized light (red solid line) and TE-polarized light (blue dotted line). The black solid line is a Gaussian fit of the absorption with a linear baseline.

respectively. These data show that the broadening of the ISB absorption in cubic QWs is larger than in their hexagonal counterparts. For example, the FWHM is 0.17 eV, which is slightly higher than the typical broadening observed for hexagonal GaN/AlN QWs absorbing in the same spectral range (typically 60−100 meV in doped QWs (Helman et al., 2003; Tchernycheva et al., 2006) and 40 meV in undoped samples (Julien et al., 2007)). In Unuma et al. (2003) the broadening is attributed to thickness fluctuations, interface roughness and impurity scattering as in the case of GaAs/AlGaAs QWs. The large broadening in relatively wide cubic QWs may be due to fluctuations of the QW thickness, which have a stronger influence on the transition energy in the case of cubic QW than in hexagonal QW, because internal electric fields in the latter confine the carriers and make the transition energy almost thickness independent (Tchernycheva et al., 2006).

The quantum confinement in cubic QWs was modelled using an effective mass model. The PL and ISB transition energies of the QW structures were then calculated by self-consistently solving the Schrödinger and Poisson equations. These simulations allowed for the obtainment of some material parameters, e.g., the electron effective mass in cubic GaN was estimated to be close to $0.11m_0$ and the CB offset between GaN and AlN was found to be about 1.2 eV or higher. The valence-band offset (VBO) and the conduction-band offset (CBO) were also calculated using an ab-initio approach (calculating many-body corrections) within the *GW* approximation on top of hybrid-functional density functional theory calculations. A CBO of (1.4 ± 0.1) eV and a VBO of (0.5 ± 0.1) eV are obtained in good agreement with the values deduced from measured intersubband transition energies (Mietze et al., 2011).

The transmission measurements in the THz spectral region were performed at 4.7K in a Bruker Fourier transform infrared spectrometer using a glow-bar source and a liquid helium-cooled Si bolometer. The sample was cut into two pieces of same length. Both pieces were polished with 30 degrees facets and placed face-to-face under mechanical pressure on the cold finger of a liquid helium-cooled cryostat. This configuration allowed enhancing the light transmission by doubling the surface of the input facet. Placing the active QWs face-to-face also provides a good coupling of the TM-polarized THz radiation with the ISB transitions.

Fig. 6.16 shows the transmission spectrum of an $Al_{0.05}Ga_{0.95}N/GaN$ MQW structure for TM- and TE-polarized light (Machhadani et al., 2011). The transmission of the sample has been normalized to 1 at low energies. As seen in Fig. 11−16, the sample exhibits absorption peaked at 19.7 meV (4.76 THz) only for TM-polarized light, which is a clear signature of ISB absorption. The three absorption resonances between 30 and 40 meV, which are not influenced by the light polarization, are related to the SiC-on-Si substrate.

These first observations of ISB absorption at THz frequencies in cubic GaN/$Al_{0.05}Ga_{0.95}N$ QWs may open up prospects for the future development of quantum cascade lasers operating at noncryogenic temperature in this material system.

6.3.2 Cubic AlGaN/GaN Heterojunction Field-effect Transistors

Besides the impressive application of group III-nitrides in optoelectronics, the number of electronic devices based on wide-gap III-nitrides is presently increasing. Due to the large band gap of GaN and AlN and their ternary compounds, they are good candidates for high-frequency and high-power devices and tremendous research activities have been undertaken to grow multilayer group III-nitride stacks in still improving crystalline perfection. Most of these activities have been devoted to group III-nitrides with wurtzite (hexagonal) crystal structure.

However, group III-nitrides can also been grown in the less energetically favourable cubic (ZB) structure, which, due to the absence of built-in electric fields, have some potential advantages over their hexagonal counterparts where built-in electric fields arising from spontaneous and piezoelectric polarization may set limits on the performance of some electronic devices. Thus, the cubic structure may be advantageous for some device applications, like normally off FETs. In addition, phonon scattering is lower in the cubic phase due to the higher crystallographic symmetry. As a result, the mobility of electrons and holes in the cubic phase is expected to be larger than in hexagonal structures.

AlGaN/GaN HFETs are of interest for high-power and high-frequency amplifiers. This is motivated by their potential in commercial and military applications, e.g., in communication systems, radar, wireless stations, high-temperature electronics, and high-power solid-state switching. Currently, state-of-the-art HFETs are fabricated on c-plane wurzite AlGaN/GaN heterostructures. Their inherent polarization fields produce extraordinary large sheet carrier concentrations at the AlGaN/GaN hetero-interface which are advantageous for normally-on-type transistors (Rajan et al., 2004; Haffouz et al., 2005; Choi et al., 2007).

However, for switching devices and digital electronics, FETs with normally off characteristics are desirable. It was discussed by Abe et al. (2006) that the use of cubic III-nitrides would offer fabricating HFETs without parasitic polarization fields and with equal electrical properties for all gate orientations. Further, with cubic nitrides the same technology for the production of normally on and normally off devices can be applied. A first demonstration of a c-nitride HFET with normally off characteristics with a threshold voltage of $V_{th} = 0.6$V has recently been reported by Tschumak et al. (2010).

For the epitaxy of cubic AlGaN/GaN heterostructures, free-standing Ar^+ implanted 3C-SiC (001) substrates were used. A three-energy implantation with Ar^+ ions at doses of $6 \times 10^{14}\,cm^{-2}$ at 160 keV, $2.4 \times 10^{14}\,cm^{-2}$ at 80 keV and $1.2 \times 10^{14}\,cm^{-2}$ at 40 keV was applied to form an isolating damage layer near the surface. The c-AlGaN/GaN layer stacks consist of 200-nm unintentionally doped (UID) cubic GaN (c-GaN) followed by 4-nm UID cubic $Al_{0.33}Ga_{0.67}N$ (c-$Al_{0.33}Ga_{0.67}N$) spacer layer, 6-nm-thick c-$Al_{0.33}Ga_{0.67}N$ doped with $N_D = 4 \times 10^{18}\,cm^{-3}$ Si and 10-nm UID c-$Al_{0.33}Ga_{0.67}N$. The RMS roughness of the c-$Al_{0.33}Ga_{0.67}N$ surface measured by AFM was 3 nm. The dislocation density of c-GaN was about $5 \times 10^{9}\,cm^{-2}$ as estimated from the FWHM of the X-ray rocking curve of the (002) c-GaN reflex. Thus, the crystalline properties of the c-AlGaN/GaN heterostructures were comparable with those of hexagonal *a*-plane structures (Kuroda et al., 2007).

Ti/Al/Ni/Au (15 nm/50 nm/15 nm/50 nm) was thermally evaporated and annealed at 850°C for 30 seconds in nitrogen atmosphere to form source and drain contacts with ohmic characteristics. Then, c-AlGaN/GaN mesas were formed by $SiCl_4$ reactive ion etching (RIE) in order to separate single devices. Gate fingers were fabricated by evaporation of Pd/Ni/Au (15 nm/15 nm/50 nm) and subsequent annealing at 400°C for 10 minutes. The devices had a gate length of 2 μm, a gate width of 25 μm, and a source-to-drain spacing of 8 μm. Finally, contact pads were thermally evaporated onto a 250-nm-thick SiO_2 layer which was deposited around the FET devices for isolation.

Fig. 6.17 shows the room-temperature DC drain current−voltage (IV) curves of a c-HFET, revealing a clear field effect when the gate-to-source voltage is varied from −1V to +2V. A parasitic shunt current $I_{shunt} = 0.34\,mA\,mm^{-1}$ was observed at $V_{DS} = 10$V. It is most likely caused by insufficient isolation between the device and the high conductive 3C-SiC substrate. The source-to-drain current difference between $V_G = -1$V and $V_G = +2$V was $0.5\,mA\,mm^{-1}$ which is 20 times lower than the source-to-drain current of *a*-plane AlGaN/GaN HFET with a (As, 2003, 2009; As et al., 1997, 2003, 2006; Northrup et al., 2000; Koblmüller et al., 2005; Brandt et al., 2004; Schikora et al., 1996, 2000; Feuillet et al., 1997; Neugebauer et al., 1998, 2003; Schörmann et al., 2006a,b, 2007; Mula et al., 2001; Adelmann et al., 2002; Gogneau et al., 2004; Lischka, 1997; Yang et al., 1996; Okumura et al., 1997; Yang et al., 1999; Ayers, 1995; Daudin et al., 1998; Daudin and Widmann, 1997; Lebedev et al., 2005; Schupp et al., 2010a,b,c,d; Braun, 1999; Holy, 1999;

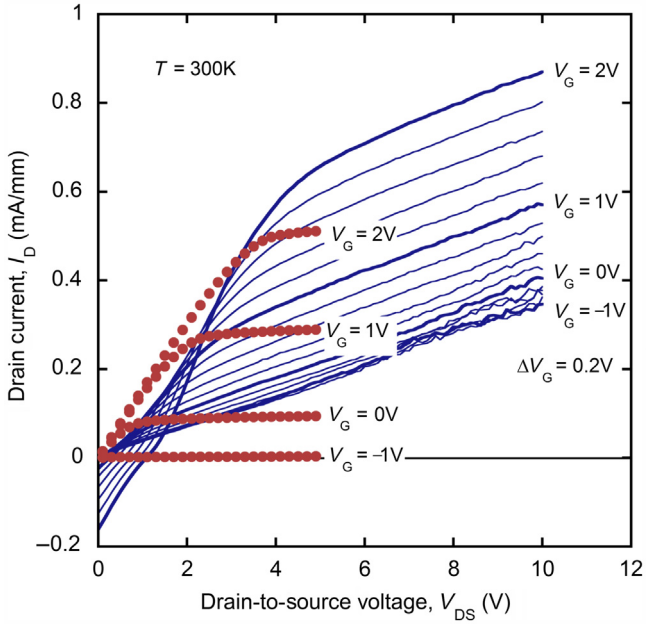

FIGURE 6.17 Static output characteristics of a fabricated cubic AlGaN/GaN HFET. The dotted lines represent calculated output characteristics at $V_G = -1$, 0, +1 and +2V.

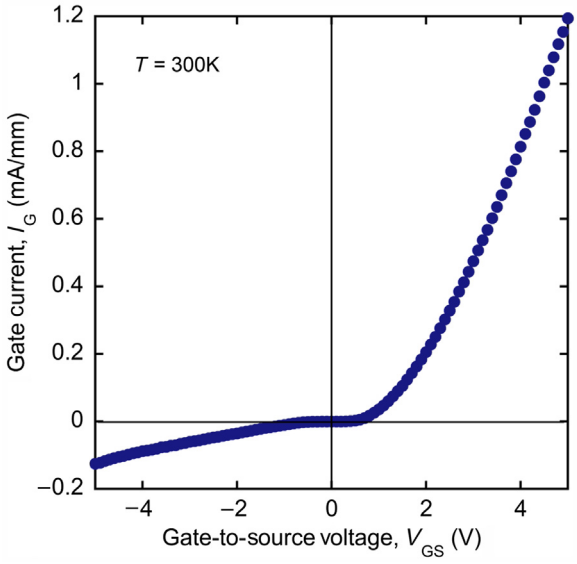

FIGURE 6.18 Room temperature I–V characteristics of the gate contact.

Cobet et al., 2009; Goldhahn, 2003; Röppischer et al., 2009; Leute et al., 2009; Bechstedt et al., 2005; Craven et al., 2004; Grandjean et al., 1999; Kindel et al., 2009, 2010; Bardoux et al., 2006, 2008; Simeonov et al., 2008; Kako et al., 2004, 2003, 2006; Bretagnon et al., 2006; Ostapenko et al., 2012; Simon et al., 2003; Martinez-Guerrero et al., 2000; Bürger et al., 2012, 2015; Taylor and Jones, 1960; Strite et al., 1991; Frank and Van der Merwe, 1949; Schmid, 2006; Fonoberov and Balandin, 2003; Leonard et al., 1994; Stranski and Krastanow, 1937; Arakawa et al., 2003; Kemper et al., 2014; Koguchi, 2007; Sanorpim et al., 2007; DeCuir et al., 2006; Hofstetter et al., 2006; Guillot et al., 2006; Baumann et al., 2005; Ridley et al., 2003; Suzuki et al., 2003; Vurgaftman et al., 2001; Morkoc, 1999; Andersson et al., 2007; Ambacher et al., 1999; Park and Chuang, 2000; Gmachl and Ng, 2003; Kuokstis et al., 2005; DeCuir et al., 2008; Machhadani et al., 2011; Helman et al., 2003; Tchernycheva et al., 2006; Julien et al., 2007; Unuma et al., 2003; Mietze et al., 2011; Rajan et al., 2004; Haffouz et al., 2005; Choi et al., 2007; Abe et al., 2006; Tschumak et al., 2010; Kuroda et al., 2007; ATLAS, 2008; Zado et al., 2011; Adivarahan et al., 2005; Gila et al., 2001; Zado et al., 2012a,b; Sergent et al., 2013; Kako et al., 2003) gate orientation (Kuroda et al., 2007). It was suggested in Tschumak et al. (2010) that this difference is mainly due to the relatively high resistivity of the source and drain contacts of $\rho_C = 150\ \Omega$cm, which have not yet been optimized.

From the gate contact I–V characteristics shown in Fig. 6.18, it was concluded that (1) the negative drain current at $V_{DS} = 0$V and $V_G > 1$V is caused by gate leakage in forward direction and (2) the drain current of 0.34 mA mm^{-1} at $V_{DS} = 10$V and $V_G = 0$V is mainly due to reverse gate leakage ($I_G = 0.3$ mA mm^{-1} at $V_{DS} = 10$V and $V_G = 0$V).

From the output characteristics, the field-dependent electron mobility at the c-AlGaN/GaN interface was estimated. It is slightly smaller than the Hall mobility of *a*-plane AlGaN/GaN FETs where a maximum mobility of 46 cm^2 Vs^{-1} was measured (Kuroda et al., 2007).

The output characteristics of these first cubic HFET devices were calculated using the two-dimensional device simulator ATLAS (ATLAS, 2008). The parameters used in the simulation were a 3C-SiC substrate with zero conductivity followed by 200-nm c-GaN buffer layer, a 4-nm c-$Al_{0.33}Ga_{0.67}N$ spacer layer with $N_D = 4 \times 10^{17}$ cm^{-3}, a 6-nm layer with $N_D = 4 \times 10^{18}$ cm^{-3} and a 10-nm cap layer with $N_D = 4 \times 10^{17}$ cm^{-3}. A donor concentration of $N_D = 4 \times 10^{16}$ cm^{-3} and an electron mobility of 5 cm^2 Vs^{-1} at the c-AlGaN/GaN interface were assumed. Further, a linear decrease in the donor concentration and mobility with increasing distance from the surface had to be taken into account to fit best the experimental data. This assumption seems reasonable since it has been shown in As et al. (2006) that the dislocation density of c-GaN layers increases with decreasing distance to the substrate–layer interface. The contact

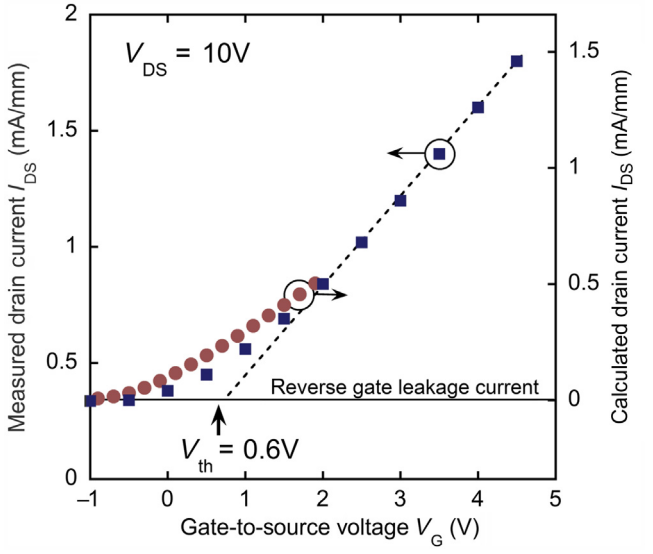

FIGURE 6.19 Measured (squares) and calculated (solid circles) transfer characteristics of a cubic $Al_{0.33}Ga_{0.67}N$/GaN HFET at drain-to source voltage of $V_{DS} = 10V$. The right-hand scale of the calculated data is shifted for the value of the reverse gate leakage current of 0.34 mA/mm measured at $V_G = -1V$.

resistivity of the source and drain contacts was set to $\rho_C = 150\ \Omega$cm. The Schottky gate contact with a barrier height of 0.8 eV was localized on top of the c-AlGaN layer. Like in the realized HFET devices, the gate length was 2 μm and the gate-to-source and gate-to-drain spacing was 3 μm. Unfortunately, it was not possible to include the effect of gate leakage in the simulation. The dotted lines in Fig. 6.17 represent the calculated drain current I_D of the HFET at $V_G = -1V$, 0V, 1V and 2V, respectively. The increase in the calculated drain current with increasing V_G is in good agreement with the measured data. However, experimental data show a drain current at $V_G = 0V$ which is not found in the simulation. It was concluded that the measured drain current is due to gate leakage in reverse direction.

The measured (squares, left-hand scale) and calculated (circles, right-hand scale) transfer characteristics of the cubic HFET at $V_{DS} = 10V$ are depicted in Fig. 6.19. The calculated data are shifted with respect to the experimental data since the current measured at $V_G = -1V$ is mainly due to gate leakage, which has not been included in the simulation. The threshold voltage $V_{th} = 0.6V$ was obtained from the intersection of the extrapolated experimental drain current data and the gate leakage line (0.34 mA mm^{-1}). Thus, the electron channel at the c-AlGaN/GaN interface is controlled by positive gate bias. These results clearly demonstrate that cubic AlGaN/GaN may be used for fabrication of HFETs with normally off characteristics.

Obviously, the first demonstrators of cubic nitride HFETs (Tschumak et al., 2010) had output characteristics which are influenced by deficiencies in the structures as given in the following:

1. A large shunt current through the GaN buffer layer. Capacitance–voltage measurements on nominally undoped cubic GaN revealed a doping concentration in the order of 2×10^{17} cm^{-3}, yielding a drain current of 0.3 mA mm^{-1} at $V_g = 0V$ and $V_{DS} = 10V$. As a consequence, experiments were performed to reduce the background doping of MBE grown c-GaN. Zado et al. (2011) used carbon acceptors supplied by a CBr_4 sublimation source connected to the MBE chamber to compensate donors. No carrier gas was used and the CBr_4 flux was set by a high-precision needle valve at constant source temperature of 20°C. They were able to vary the concentration of incorporated carbon acceptors by more than two orders of magnitude. In this way, the concentration of residual donors was compensated and a decrease of the conductance of c-GaN:C by two orders of magnitude was demonstrated.
2. The high gate leakage current of HFETs. It is undesirable for high-power and low-noise applications, and severely reduces the performance of HFETs.

The use of metal/insulator layers, instead of a Schottky gate, leading to the metal–insulator–semiconductor heterojunction field-effect transistors (MIS-HFETs), may improve the device characteristics (Adivarahan et al., 2005; Gila et al., 2001). Zado et al. (2012a) have fabricated different MIS structures on cubic GaN. They compared the trap energies and trap densities of devices produced by ex-situ plasma-enhanced chemical vapour deposition and in-situ by MBE. In the first series, the 600-nm-thick c-GaN layers were taken out from the MBE chamber and Si_3N_4 layers were deposited by plasma-enhanced chemical vapour deposition (PECVD) at a substrate temperature of 300°C. The pressure during the deposition was 1.33 mbar and the deposition rate was 16 nm/min. The deposited insulator thickness was estimated from the saturation region of the CV curves assuming a dielectric constant of 7.5 for Si_3N_4 (Zado et al., 2012a,b). In a second series, Si_3N_4 layers were deposited in-situ in the MBE chamber after the growth of the c-GaN buffer using the nitrogen plasma source and a silicon thermal evaporation source. The substrate temperature for the deposition of Si_3N_4 layers was 300°C and the growth rate was 13 nm h^{-1}. The trap energy and trap densities in MIS structures produced in-situ by MBE and ex-situ by plasma-enhanced chemical vapour deposition were compared. The MBE-produced structure showed a reduced hysteresis effect in

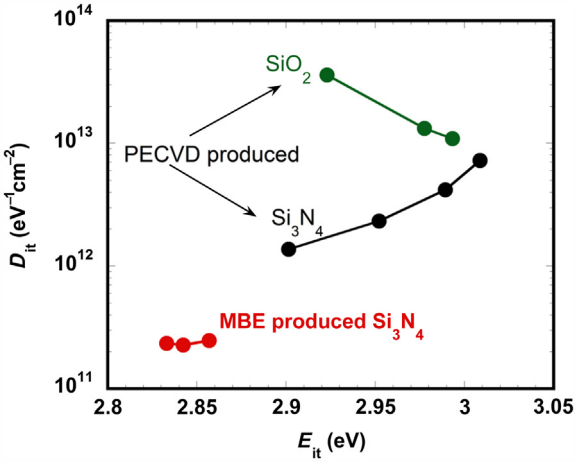

FIGURE 6.20 The interface state density D_{it} at the GaN/insulator interface versus energy E_{it} above the valence band edge of c-GaN.

the CV curve, indicating a lower density of mobile charges. By admittance spectroscopy, interface traps were detected between 0.2 and 0.4 eV below the conduction-band edge with a minimum defect density of $D_{it} = 2.5 \times 10^{11}\,\mathrm{cm}^{-2}\,\mathrm{eV}^{-1}$ (see Fig. 6.20). This is more than one order of magnitude lower than in PECVD-produced Si_3N_4 structures, and two orders of magnitude lower than that measured with SiO_2 insulator layers. These findings demonstrate that MBE-produced in-situ Si_3N_4 layers can lead to a reasonable decrease of the gate current in further HFET structures.

6.3.3 Cubic GaN/AlN Quantum Dots for Single Photon Emission

QDs were grown by PA-MBE on a 3C-SiC/Si(100) substrate. For the purpose of probing the emission from an individual QD, submicron-scale mesas were processed on the sample. The optical properties of the QDs were then measured using microphotoluminescence spectroscopy, with nonresonant excitation via a frequency-tripled Ti:Sapphire pulsed laser (200 fs pulses at 80 MHz with an excitation wavelength of 266 nm). The laser was focused to an elliptical spot (10 × 40 μm) at a steep angle of 60° to the normal of the sample plane. The luminescence from the QDs was then collected by a microscope objective (N.A. = 0.4). The objective was followed by concave mirrors with a pinhole to spatially filter the collected light, which was then sent to a monochromator equipped with both a liquid-nitrogen cooled CCD camera to analyze the spectrum, and a Hanbury–Brown Twiss (HBT) setup (a 50/50 beam-splitter and two photomultiplier tubes) to perform either time-resolved PL (TRPL) studies, or photon autocorrelation measurements. The sample was held in a continuous flow helium cryostat, which enabled control of the temperature from 4K to room temperature.

The emission from the QD ensemble, measured on unpatterned areas of the sample, exhibits a Gaussian distribution centred around 3.5 eV with about 200 meV full-width at half-maximum (Sergent et al., 2013). Isolated single emission lines can be found on the higher energy side of the QD ensemble PL between 3.5 and 4.3 eV, when probing submicron-scale mesas (Sergent et al., 2013). The emission of a single cubic GaN QD at 3.687 eV had a linewidth of 2.1 meV (see Fig. 6.21A). The linewidth is reasonably broad, most likely due to spectral diffusion, which may be enhanced by the presence of an internal field, and interaction between the exciton in the QD and surface defects on the mesa side walls. TRPL studies were performed based on time-correlated single-photon counting, with 230 ps time resolution, by using one of the arms of the HBT setup, and a trigger signal from the excitation pulsed laser. Fig. 6.21B shows the PL decay. The lifetime of this particular QD is 360 ps, which is about one order of magnitude shorter than those typically measured from polar GaN QDs emitting at the same energy (Kako et al., 2003). The lifetime of 360 ps is in fair agreement with previous reports on cubic GaN QDs (Simon et al., 2003). To confirm the single-photon statistics of the emission from the QDs, we performed photon-autocorrelation mea- surement using the HBT setup. A histogram of the relative delay ($\tau = t_1 - t_2$) between a photon-detection event in one HBT arm at t_1 and in the other arm at t_2, is proportional to the second order coherence function $g^{(2)}[\tau]$. A measurement $g^{(2)}[0] < 0.5$ verifies the detection of a single photon (an $n = 1$ Fock state) from a single quantum emitter. Fig. 6.21D shows such an autocorrelation histogram, measured at 4K. The suppression of counts at $\tau = 0$ is a clear evidence for the single photon nature of the emission. The second order coherence function of the peak at zero time delay, $g^{(2)}[0]$ is 0.25. The $g^{(2)}[0]$ is the coincidence counts peak area for $-T/2 < \tau < T/2$, normalized to the average counts of the surrounding peaks, where T is the repetition period of the pulsed excitation. The $g^{(2)}[0]$ value becomes 0.05 when corrected for background and detector dark counts (Bounouar et al., 2012).

6.4 CONCLUSIONS

Recent developments of the in-situ control of growth conditions during the MBE of cubic III-nitrides (GaN/AlN) paved the way for the production of layer stacks with high phase purity and severely improved

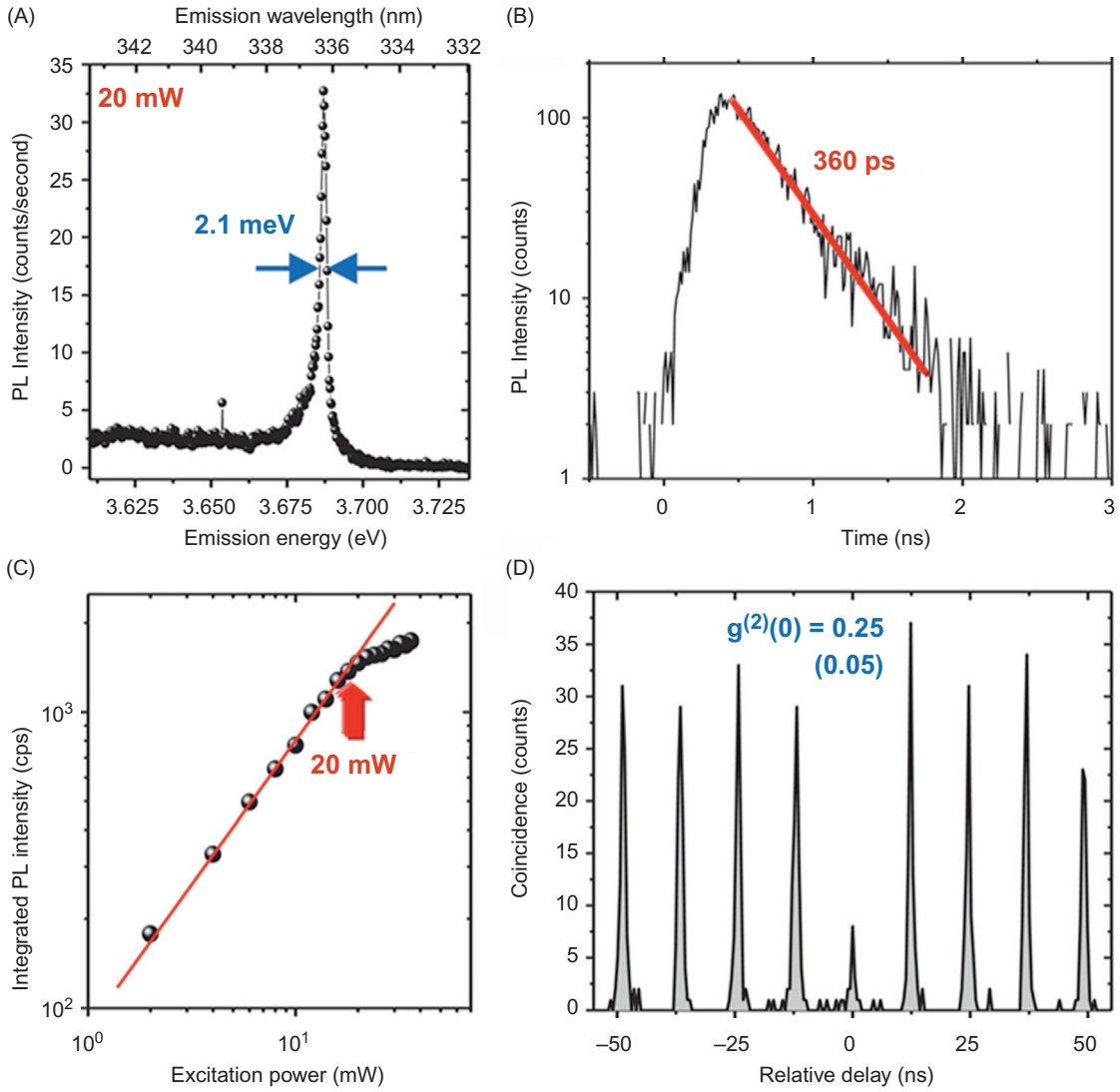

FIGURE 6.21 (A) Emission spectrum of a single cubic GaN QD measured at 4K with an excitation power of 20 mW. (B) PL decay trace of this particular dot measured at 4K. (C) Excitation power dependence of the QD at 4K. The red line shows the linear dependence of the PL intensity at excitation powers < 20 mW. (D) Autocorrelation histogram of this particular QD at 4K and an excitation power of 20 mW. The number in the bracket is the background corrected value of $g^{(2)}[0]$.

structural properties. Group III-nitride nanostructures are free from any polarization fields due to their cubic crystal symmetry and, therefore, may be considered as the true nonpolar group III-nitrides and, thus, are the ideal material basis of devices where polarization fields are detrimental for their performance. First demonstrators are HFETs with both normally on and normally off operation mode, MQWs for intersubband absorption in the near infrared up to the terahertz spectral region and single photon emitting cubic GaN QDs. Their properties are summarized in this paper indicating a clear potential of nonpolar cubic III-nitrides for further applications.

Acknowledgments

The authors want to thank E. Tschumak, T. Schupp, C. Mietze, A. Zado, S. Potthast, J. Schörmann, M. Bürger, and Prof. W.G. Schmidt and E. Rauls at University of Paderborn, Prof. F. Julien and M. Tchernycheva at University Paris-Sud, Prof. M.O. Manasreh and E. DeCuir, Jr. at Arkansas State University, J. Gerlach at IOM Leipzig, J. Pezoldt, F. Schwierz, and P. Schley at University of Ilmenau, Prof. R. Goldhahn at University of Magdeburg, and Prof. Y. Arakawa, S. Sergent, and S. Kako at the University of Tokyo. My special regards are expressed to Dr. M. Abe and Dr. H. Nagasawa at HOYA Corporation for the supply of excellent 3C-SiC substrates and the financial support by DFG (project AS 107/4-1 and within the research group "Micro- and Nanostructures in Optoelectronics and Photonics" GRK 1464).

References

Abe, M., Nagasawa, H., Potthast, S., Fernandez, J., Schörmann, J., As, D.J., et al., 2006. IEICE Trans. Electron. E89-C, 1057.

Adelmann, C., Brault, J., Jalabert, D., Gentile, P., Mariette, H., Mula, G., et al., 2002. J. Appl. Phys. 91, 9638.

Adivarahan, V., Yang, J., Koudymov, A., Simin, G., Asif Khan, M., 2005. IEEE Electron. Dev. Lett. 26, 535.

Ambacher, O., Dimitrov, R., Stutzmann, M., Foutz, B.E., Murphy, M. J., Smart, J.A., et al., 1999. Phys. Stat. Sol. B 216, 381.

Andersson, T.G., Liu, X.Y., Aggerstam, T., Janes, P., Holmstrom, P., Lourdudoss, S., et al., 2007. J. Cryst. Growth 301–302, 457.

Arakawa, Y., Miyamura, M., Tachibana, K., Hoshimo, K., Kako, S., 2003. Inst. Phys. Conf. Ser. 171, 61.

As, D.J., 2003. In: Manasreh, M.O. (Ed.), Optoelectronic Properties of Semiconductors and Superlattices, vol. 19. Taylor & Francis, New York, pp. 323–450. , Chap. 9.

As, D.J., 2009. Microelectron. J. 40, 204.

As, D.J., Schmilgus, F., Wang, C., Schöttker, B., Schikora, D., Lischka, K., 1997. Appl. Phys. Lett. 70, 1311.

As, D.J., Potthast, S., Köhler, U., Khartchenko, A., Lischka, K., 2003. MRS Symp. Proc. 743 (L5), 4.

As, D.J., Potthast, S., Schörmann, J., Li, S.F., Lischka, K., Nagasawa, H., et al., 2006. Mater. Sci. Forum 527–529, 1489.

ATLAS User's Manual—Device Simulation Software, Salvaco International, 2008.

Ayers, J.E., 1995. J. Appl. Phys. 78, 3724.

Bardoux, R., Guillet, T., Lefebvre, P., Taliercio, T., Bretagnon, T., Rousset, S., et al., 2006. Phys. Rev. B 74, 195319.

Bardoux, R., Guillet, T., Gil, B., Lefebvre, P., Bretagnon, T., Talierco, T., et al., 2008. Phys. Rev. B 77, 235315.

Baumann, E., Giorgetta, F.R., Hofstetter, D., Lu, H., Chen, X., Schaff, W.J., et al., 2005. Appl. Phys. Lett. 87, 191102.

Bechstedt, F., Seino, K., Hahn, P.H., Schmidt, W.G., 2005. Phys. Rev. B 72, 245114.

Bounouar, S., Elouneg-Jamroz, M., Hertog, M.D., Morchutt, C., Bellet-Amalric, E., André, R., et al., 2012. Nano Lett. 12, 2977.

Brandt, O., Sun, Y.J., Däweritz, L., Ploog, K.H., 2004. Phys. Rev. B 69, 165326.

[Applied RHEED] Braun, W., 1999. Springer tracts in Modern Physics, 154. Springer, Berlin.

Bretagnon, T., Lefebvre, P., Valvin, P., Bardoux, R., Guillet, T., Taliercio, T., et al., 2006. Phys. Rev. B 73, 113304.

Bürger, M., Schupp, T., Lischka, K., As, D.J., 2012. Phys. Stat. Sol. (c) 9, 1273.

Bürger, M., Lindner, J.K.N., Reuter, D., As, D.J., 2015. Phys. Stat. Sol. (c) 12, 452.

Choi, Y.C., Shi, J., Pophristic, M., Spencer, M.G., Eastman, L.F., 2007. J. Vac. Sci. Technol. B 25, 1836.

Cobet, C., Goldhahn, R., Richter, W., Esser, N., 2009. Phys. Stat. Sol. (b) 246, 1440.

Craven, M.D., Waltereit, P., Speck, J.S., DenBaars, S.P., 2004. Appl. Phys. Lett. 84, 496.

Daudin, B., Widmann, F., 1997. J. Cryst. Growth 182, 1.

Daudin, B., Feuillet, G., Hübner, J., Samson, Y., Widmann, F., Philippe, A., et al., 1998. J. Appl. Phys. 84 (4), 2295.

DeCuir, E.A., Fred, E., Passmore, B.S., Muddasani, A., Manasreh, M. O., Xie, J., et al., 2006. Appl. Phys. Lett. 89, 151112.

DeCuir Jr, E.A., Manasreh, M.O., Tschumak, E., Schörmann, J., As, D.J., Lischka, K., 2008. Appl. Phys. Lett. 92, 201910.

Feuillet, G., Hamaguchi, H., Ohta, K., Hacke, P., Okumura, H., Yoshida, S., 1997. Appl. Phys. Lett. 70, 1025.

Fonoberov, V.A., Balandin, A.A., 2003. J. Appl. Phys. 94, 7178.

Frank, F.C., Van der Merwe, J.H., 1949. Proc. R Soc. London Ser. A 198, 205.

Gila, R.B., Ren, F., Abernathy, C.R., 2001. Mater. Sci. Eng. R Rep. 44, 151.

Gmachl, C., Ng, H.M., 2003. Electron. Lett. 39, 567.

Gogneau, N., Sarigiannidou, E., Monroy, E., Monnoye, S., Mank, H., Daudin, B., 2004. Appl. Phys. Lett. 85, 1421.

Goldhahn, R., 2003. Acta Phys. Polonica A 104, 123.

Grandjean, N., Damilano, B., Dalmasso, S., Leroux, M., Laügt, M., Massies, J., 1999. J. Appl. Phys. 86, 3714.

Guillot, F., Bellet-Amalric, E., Monroy, E., Tchernycheva, M., Nevou, L., Doyennette, L., et al., 2006. J. Appl. Phys. 100, 044326.

Haffouz, S., Tang, H., Bardwell, J.A., Hsu, E.M., Webb, J.B., Rolfe, S., 2005. Solid State Electron 49, 802.

Helman, A., Tchernycheva, M., Lusson, A., Warde, E., Julien, F.H., Moumanis, K., et al., 2003. Appl. Phys. Lett. 83, 5196.

Hofstetter, D., Baumann, E., Giorgetta, F.R., Graf, M., Maier, M., Guillot, F., et al., 2006. Appl. Phys. Lett. 88, 121112.

Holy, V., 1999. High-resolution X-ray scattering from thin films and multilayers, Springer Tracts in Modern Physics, vol. 149. Springer, Berlin.

Julien, F.H., Tchernycheva, M., Nevou, L., Doyennette, L., Colombelli, R., Warde, E., et al., 2007. Phys. Stat. Sol. A 204, 1987.

Kako, S., Miyamura, M., Tachibana, K., Hoshino, K., Arakawa, Y., 2003. Appl. Phys. Lett. 83, 984.

Kako, S., Hoshino, K., Iwamoto, S., Ishida, S., Arakawa, Y., 2004. Appl. Phys. Lett. 85, 64.

Kako, S., Santori, C., Hoshino, K., Götzinger, S., Yamamoto, Y., Arakawa, Y., 2006. Nat. Mater. 5, 887.

Kemper, R.M., Mietze, C., Hiller, L., Stauden, T., Pezoldt, J., Meertens, D., et al., 2014. Phys. Stat. Sol. (c) 11, 265.

Kindel, C., Kako, S., Kawano, T., Oishi, H., Arakawa, Y., 2009. Jpn. J. Appl. Phys. 48, 04C116.

Kindel, C., Kako, S., Kawano, T., Oishi, H., Arakawa, Y., Hönig, G., et al., 2010. Phys. Rev. B 81, 241309.

Koblmüller, G., Brown, J., Averbeck, R., Riechert, H., Pongratz, P., Speck, J.S., 2005. Appl. Phys. Lett. 86, 041908.

Koguchi, N., 2007. Mater. Res. Symp. Proc. 959, 18.

Kuokstis, E., Sun, W.H., Chen, C.Q., Yang, J.W., Khan, M.A., 2005. J. Appl. Phys. 97, 103719.

Kuroda, M., Ishida, H., Ueda, T., Tanaka, T., 2007. J. Appl. Phys. 102, 093703.

Lebedev, V., Cimalla, V., Kaiser, U., Foerster, Ch, Pezoldt, J., Biskupek, J., et al., 2005. J. Appl. Phys. 97, 114306.

Leonard, D., Pond, K., Petroff, P.M., 1994. Phys. Rev. B 50, 11687.

Leute, R.A.R., Feneberg, M., Sauer, R., Thonke, K., Thapa, S.B., Scholz, F., et al., 2009. Appl. Phys. Lett. 95, 031903.

Lischka, K., 1997. Phys. Stat. Sol. (b) 202, 673.

Machhadani, H., Tchernycheva, M., Rigutti, L., Saki, S., Colombelli, R., Mietze, C., et al., 2011. Phys. Rev. B 83, 075313.

Martinez-Guerrero, E., Adelmann, C., Chabuel, F., Simon, J., Pelekanos, N.T., Mula, G., et al., 2000. Appl. Phys. Lett. 77, 809.

Mietze, C., Landmann, M., Rauls, E., Machhadani, H., Sakr, S., Tchernycheva, M., et al., 2011. Phys. Rev. B 83, 195301.

Morkoc, Hadis, 1999. Nitride semiconductors and devices, Springer Series in Materials Science, vol. 132. Springer-Verlag, p. 488.

Mula, G., Adelmann, C., Moehl, S., Oullier, J., Daudin, B., 2001. Phys. Rev. B 64, 195406.

Neugebauer, J., Zywietz, Z., Scheffler, M., Northrup, J.E., Van der Walle, C.G., 1998. Phys. Rev. Lett. 80, 3097.

Neugebauer, J., Zywietz, T.K., Scheffler, M., Northrup, J.E., Chen, H., Feenstra, R.M., 2003. Phys. Rev. Lett. 90, 056101.

Northrup, J.E., Neugebauer, J., Feenstra, R.M., Smith, A.R., 2000. Phys. Rev. B 61, 9932.

Okumura, H., Ohta, K., Feuillet, G., Balakrishnan, K., Chichibu, S., Hamaguchi, H., et al., 1997. J. Cryst. Growth 178, 113.

Ostapenko, I.A., Hönig, G., Rodt, S., Schliwa, A., Hoffmann, A., Bimberg, D., et al., 2012. Phys. Rev. B 85, 081303(R).
Park, S.-H., Chuang, S.-L., 2000. Appl. Phys. Lett. 76, 1981.
Rajan, S., Waltereit, P., Poblenz, C., Heikman, S.J., Green, D.S., Speck, J.S., et al., 2004. IEEE Electron. Dev. Lett. 25, 247.
Ridley, B.K., Schaff, W.J., Eastman, L.F., 2003. J. Appl. Phys. 94, 3972.
Röppischer, M., Goldhahn, R., Rossbach, G., Schley, P., Cobet, C., Esser, N., et al., 2009. J. Appl. Phys. 106, 076104.
Sanorpim, S., Takuma, E., Ichinose, H., Katayama, R., Onabe, K., 2007. Phys. Stat. Sol. (b) 244, 1769.
Schikora, D., Hankeln, M., As, D.J., Lischka, K., Litz, T., Waag, A., et al., 1996. Phys. Rev. B 54, R8381.
Schikora, D., Schwedhelm, S., As, D.J., Lischka, K., Litvinov, D., Rosenauer, A., et al., 2000. Appl. Phys. Lett. 76, 418.
Schmid, G., 2006. Nanoparticles: From Theory to Application. Wiley-VCH, New York.
Schörmann, J., Potthast, S., As, D.J., Lischka, K., 2006. Appl. Phys. Lett. 89, 131910.
Schörmann, J., As, D.J., Lischka, K., Schley, P., Goldhahn, R., Li, S.F., et al., 2006. Appl. Phys. Lett. 89, 261903.
Schörmann, J., Potthast, S., As, D.J., Lischka, K., 2007. Appl. Phys. Lett. 90, 041918.
Schupp, T., Meisch, T., Neuschl, B., Feneberg, M., Thonke, K., Lischka, K., et al., 2010a. AIP Conf. Proc. 1292, 165.
Schupp, T., Rossbach, G., Schley, P., Goldhahn, R., Lischka, K., As, D.J., 2010b. Phys. Stat. Sol. (c) 7, 17.
Schupp, T., Lischka, K., As, D.J., 2010c. J. Cryst. Growth 312, 1500.
Schupp, T., Meisch, T., Neuschl, B., Feneberg, M., Thonke, K., Lischka, K., et al., 2010d. J. Crystal Growth 312, 3235.
Sergent, S., Kako, S., Bürger, M., As, D.J., Arakawa, Y., 2013. Appl. Phys. Lett. 103, 151103.
Simeonov, D., Dussaigne, A., Butt'e, R., Grandjean, N., 2008. Phys. Rev. B 77, 075306.
Simon, J., Pelekanos, N., Adelmann, C., Martinues-Guerrero, E., André, R., Daudin, B., et al., 2003. Phys. Rev. B 68, 035312.
Simon, J., Pelekanos, N., Adelmann, C., Martinez-Guerrero, E., André, R., Daudin, B., et al., 2003. Phys. Rev. B 68, 035312.
Stranski, I.N., Krastanow, L., 1937. Mon.hft f. Chem. 71, 351.
Strite, S., Ruan, J., Li, Z., Salvator, A., Chen, H., Smith, D.J., et al., 1991. J. Vac. Sci. Technol. B 9, 1924.
Suzuki, N., Iizuka, N., Kaneko, K., 2003. Jpn. J. Appl. Phys. 42, 132.
Taylor, A., Jones, R.M., 1960. In: OConner, J.R. (Ed.), Silicon Carbide – A High Temperature Semiconductor. Perganmon Press, New York.
Tchernycheva, M., Nevou, L., Doyennette, L., Julien, F.H., Warde, E., Guillot, F., et al., 2006. Phys. Rev. 73, 125347.
Tschumak, E., Granzer, R., Lindner, J.K.N., Schwierz, F., Lischka, K., Nagasawa, H., et al., 2010. Appl. Phys. Lett. 96, 253501.
Unuma, T., Yoshita, M., Noda, T., Sakaki, H., Akiyama, H., 2003. J. Appl. Phys. 93, 1586.
Vurgaftman, I., Meyer, J.R., Ram-Mohan, L.R., 2001. J. Appl. Phys. 89, 5815.
Yang, H., Brandt, O., Ploog, K., 1996. J. Electron. Mater. 25 (5), 787.
Yang, H., Zheng, L.X., Li, J.B., Wang, X.J., Xu, D.P., Wang, Y.T., et al., 1999. Appl. Phys. Lett. 74 (17), 2498.
Zado, A., Tschumak, E., Gerlach, J., Lischka, K., As, D.J., 2011. J. Cryst. Growth 343, 88.
Zado, A., Lischka, K., As, D.J., 2012a. Phys. Stat. Sol. (c) 9, 1088.
Zado, A., Gerlach, J., As, D.J., 2012b. Semicond. Sci. Technol. 27, 035020.